# Nickel isotopes and rare earth elements systematics in marine hydrogenetic and hydrothermal ferromanganese deposits

Bleuenn Guéguen, Olivier Rouxel, Yves Fouquet

# Nickel isotopes and rare earth elements systematics in marine hydrogenetic and hydrothermal ferromanganese deposits

Bleuenn Gueguen[1,2*], Olivier Rouxel[3], and Yves Fouquet[3]

[1]CNRS, Univ Brest, UMS 3113, F-29280 Plouzané, France

[2]CNRS, Univ Brest, UMR 6538 Laboratoire Géosciences Océan, F-29280 Plouzané, France

[3]IFREMER, Centre de Brest, Unité Géosciences Marines, F-29280 Plouzané, France

Submitted to *Chemical Geology*

Keywords: Nickel isotopes; marine ferromanganese deposits; hydrothermal Fe-Mn deposits; isotope fractionation

**Corresponding author:*
bleuenn.gueguen@univ-brest.fr (B. Gueguen)

**Abstract**

Attention is now being given to Ni isotope systematics in hydrogenetic marine ferromanganese (Fe-Mn) crusts as paleoceanographic proxies. Previous work focused on identifying both mineralogy (post-depositional) and source effects (Gall et al., 2013; Gueguen et al., 2016), in particular regarding hydrothermal inputs in the oceans and the response of Ni isotope biogeochemical cycling through time. The most important sink for Ni in the oceans is the Fe-Mn oxides sink, but estimation of its Ni isotope composition is only based on hydrogenetic Fe-Mn crusts. In this study, we investigated a range of Fe-Mn deposits including Fe-Mn deposits variably affected by hydrothermal inputs, including hydrothermal deposits from the Lau back-arc basin (South West Pacific) and Lo'ihi seamount (Hawaii), hydrogenetic crust and nodules from the Bauer Basin (Pacific Ocean). Nickel isotope ratios were measured by multi-collector inductively coupled plasma mass spectrometer (MC-ICP-MS) using a double-spike ($^{61}$Ni and $^{62}$Ni) correction method. The combination of Ni isotopes and rare earth element (REE) geochemistry show that Ni isotope fractionation in Fe-Mn deposits is essentially controlled by formation processes of the deposits (such as the rate of formation, the initial Mn-phase and sorption processes) which are also related to the depositional environment. Consistent with previous studies, pure hydrogenetic crusts are characterized by isotopically heavy Ni isotope signatures ($\delta^{60/58}$Ni values range from ‰ 0.9 and 2.5 ‰) and well-developed positive Ce anomalies. In contrast, mixed hydrothermal-hydrogenetic crust and nodules from the Bauer Basin (East Pacific) display negative Ce anomaly and lighter $\delta^{60/58}$Ni values (0.3 ‰ to 0.4 ‰), which are interpreted as the result of far-field hydrothermal inputs of Fe-Mn precipitates from the East Pacific Rise.

Nickel in hydrothermal deposits from the Lau Basin (0.5 and 1.1 ‰) and Lo'ihi seamount (-0.8 to -1.5 ‰) is isotopically lighter than in hydrogenetic Fe-Mn crusts. Light $\delta^{60/58}$Ni values in Lo'ihi deposits is due to the removal of Ni during Ni adsorption from seawater and from

63 the hydrothermal fluid (between 0-1.4 ‰) on Fe-oxides followed by isotope fractionation
64 between the fluid and the mineral phase. Results suggest that Ni isotopes in hydrothermal Fe-
65 rich deposits are strongly fractionated relative to the seawater/fluid source due to partial
66 removal of Ni on Fe-phases. Hydrothermal Mn-oxides deposits from the Lau Basin acquired
67 their Ni isotope signature through Ni adsorption and continuous exchange of Ni with
68 seawater. We propose that the systematic difference in Ni isotope signatures between
69 hydrogeneous and hydrothermal Fe-Mn deposits is related to the mechanisms of Ni uptake
70 into oxide minerals (e.g., birnessite vs. todorokite; Fe-oxides vs. Mn-oxides) which depend on
71 the rate of formation and the source of Mn and Fe to marine ferromanganese deposits (i.e.,
72 depositional environment) rather than Ni sources.

## 1. Introduction

Understanding the biogeochemical cycling of trace metals in the marine environment is important because they are involved in key biological reactions such that variations of metal distribution in time and space in the oceans could have significant impact on the biological pump (Price and Morel, 1991; Saito et al., 2003; Morel et al., 2014). Recent advances on hydrothermal research and metal distribution in deep water have highlighted the importance of hydrothermal venting on, for example, the iron marine geochemical budget (Toner et al., 2009; Tagliabue et al., 2010; Saito et al., 2013; Conway and John, 2014; Fitzsimmons et al., 2014; German and Seyfried, 2014; Tagliabue et al., 2014; Horner et al., 2015; Rouxel et al., 2016). Other transition metals like zinc, nickel, cadmium and copper may also be impacted by deep hydrothermal venting to various extents (e.g., John et al., 2008; Gall et al., 2013; Hannington, 2013; Little et al., 2014). Growing interest is now given to nickel (Ni) isotope systematics in Fe-Mn crusts as a potential tracer of the evolution of the biogeochemistry of trace metals in oceans through time (Gall et al., 2013; Cameron and Vance, 2014; Gueguen et al., 2016).

Marine ferromanganese (Fe-Mn) oxide deposits are ubiquitous in the oceans, and these chemically precipitated sediments represent an important sedimentary archive of trace metal seawater composition. Ferromanganese oxide deposits show a range of metal enrichment (Ni, Cu, Co) based on their geological settings, formation rates and sources of dissolved Fe, and Mn. They are commonly classified using a ternary diagram composed of iron (Fe), manganese (Mn) and (nickel (Ni) + copper (Cu) + cobalt (Co)) concentrations as the three variables in the diagram (Bonatti et al., 1972). This representation allows the discrimination between the hydrothermal, hydrogenetic and diagenetic fields (Bonatti et al., 1972) indicating different geological settings, i.e., hydrothermal environment, strictly precipitated from seawater, and dominated by diagenetic processes. Hydrogenetic ferromanganese crusts are precipitated on

volcanic seamounts at depths between 400 and 4000 m at very slow rates of 1-6 mm/Ma (Hein et al., 2003; Hein and Koschinsky, 2014). They are generally considered to be good proxies of deep seawater metal isotope composition, providing that fractionation processes during metal uptake are sufficiently well constrained. Accordingly, Fe-Mn crusts have attracted considerable interest for investigating seawater composition over a time-scale of several million years (O'Nions et al., 1998; Frank et al., 1999; Reynolds et al., 1999; Frank, 2002; Frank et al., 2002; van de Flierdt et al., 2004; Klemm et al., 2005; Klemm et al., 2007; Nielsen et al., 2011).

Initial Ni isotope composition of hydrogenetic Fe-Mn crusts reported by Gall et al. (2013) and Gueguen et al. (2016) ranges from 0.9 to 2.5 ‰ for a period of more than 60 Ma, suggesting that deep seawater Ni isotope composition could have changed in the past. Both studies investigated the Ni isotope composition of Fe-Mn crusts from the Pacific Ocean by sub-sampling Fe-Mn crusts layers through stratigraphic depth in order to evaluate the variability of Ni isotopes in seawater through time. Gall et al. (2013) suggested that Ni isotopes in seawater are sensitive to variations of Ni sources such that Ni isotopes in Fe-Mn crusts formed close to continental margins are influenced by continental weathering, and that hydrothermal inputs could also affect the Ni isotope composition of oceanic basins. It is now well established that dissolved Ni in seawater is isotopically heavier (~1.44 ±0.15 ‰; Cameron and Vance, 2014; Wang et al., 2019; Archer et al., 2020) compared to the average $\delta^{60/58}$Ni crustal value (BSE, Bulk Silicate Earth) estimated to about 0.12 ±0.01 ‰ (Klaver et al., 2020). Nickel in the oceans is mostly coming from the riverine input and has an average $\delta^{60/58}$Ni value of 0.8 ‰ (Cameron and Vance, 2014), which is heavier than the average crustal value of 0.12 ± 0.01 ‰ (Klaver et al., 2020). The affinity of Ni towards Mn oxides has been well recognized (e.g.; Koschinsky and Halbach, 1995; Koschinsky and Hein, 2003; Peacock and Sherman, 2007a; Peacock and Sherman, 2007b) and provide the main sink of Ni in

seawater. However, an estimate of the global Ni isotope composition of Fe-Mn deposits as a proxy of the Mn sink yield $\delta^{60/58}$Ni values in the range of oceanic values and even slightly heavier (Gall et al., 2013; Gueguen et al., 2016) providing no leverage to affect Ni isotope composition of seawater. As recently discussed by Archer et al. (2020) and (Little et al., 2020), the isotopic and elemental budget of Ni in the oceans is imbalanced (Cameron and Vance, 2014; Vance et al., 2016; Ciscato et al., 2018). If the ocean is at steady-state, three possibilities can explain this imbalance, (1) there is a missing isotopically heavy Ni source, (2) a light Ni sink is required, or (3) Fe-Mn crusts do not provide an accurate estimate of the marine Mn sink for Ni isotopes. A possible sink for light Ni isotopes in the ocean could be sediments rich in organic matter such as sediments deposited in continental margins and anoxic basins (Takano et al., 2017; Ciscato et al., 2018; Archer et al., 2020). However, the extent of Ni isotope fractionation is rather small (between 0 to 0.3 ‰), and the size of such reservoir is not sufficient to exert a significant control on oceanic Ni isotope budget. Based on results from Ni isotopes in metalliferous sediments from MANOP site in the East Pacific, Little et al. (2020) estimated that an isotopic Ni benthic flux extremely heavy of ~3 ‰ would balance the marine Ni budget leaving a residual light Ni reservoir in sedimentary authigenic phases.

Although some significant efforts have been undertaken for measuring Ni isotope composition of major oceanic Ni sources (Cameron and Vance, 2014; Vance et al., 2016; Ciscato et al., 2018; Little et al., 2020) and mechanisms of isotope fractionation processes (Wasylenki et al., 2015; Gueguen et al., 2018; Sorensen et al., 2020), the Ni isotope composition of the oceanic Ni sink associated with Mn oxides needs to be better understood, and it is yet unclear whether secular Ni isotope variations in marine Fe-Mn deposits may result from source effects (e.g., circulation of water masses, local inputs (diagenetic vs. hydrothermal sources)), fractionation processes during Ni incorporation in the deposits, or a

combination of both. More particularly, the effect of hydrothermal inputs on the Ni sink in Fe-Mn deposits has to be better understood.

The purpose of this work is to investigate in a range of mixed hydrothermal-hydrogenetic Fe-Mn deposits the Ni isotope composition of the Mn sink by evaluating, (1) the processes controlling the Ni isotope composition in marine Fe-Mn deposits (e.g., depositional environment, formation rates, mineralogy, source effects), and (2) the Ni isotope signature of hydrothermal Fe-Mn deposits as a proxy of the impact of hydrothermal inputs on the Ni biogeochemical cycling in the marine environment. To help our understanding of Ni isotopes in Fe-Mn deposits, we will combine Ni isotopes and rare earth elements geochemistry. Rare earth elements provide another source of information regarding metal sources and deposition rates of seafloor Fe-Mn deposits. They behave coherently in natural environments with the exception of Ce (and Eu), and relative REEs abundances are not fractionated from their source during scavenging and precipitation processes. The contrasting behavior of Ce compared to other REEs is due to the oxidation of soluble Ce(III) to insoluble Ce(IV) at the oxide surface after its sorption to the mineral surface implying that the oxidized Ce(IV) no longer exchanges with seawater (e.g.; Bau et al., 2014). Accordingly, the slow growth rates of Fe-Mn crusts allows the accumulation of more Ce in comparison to other REEs (Bau, 1999; Bau and Koschinsky, 2009; Bau et al., 2014), and they display a positive Ce anomaly. Because the rate of precipitation of hydrothermal Fe-Mn oxide deposits is rapid, hydrothermally precipitated REEs preserve the negative Ce anomaly characteristic of seawater (De Baar et al., 1985; Elderfield et al., 1988; Kuhn et al., 1998; Mills et al., 2001). Other studies also suggest that Ce oxidation could occur through similar pathways as microbial Mn oxidation in the marine environment (Moffett, 1990; Moffett, 1994). Previous studies have shown a trend between the magnitude of the Ce anomaly and the distance of Fe-Mn deposits from hydrothermal sources, with samples located further away from the

hydrothermal source and precipitated more slowly displaying higher positive Ce anomalies than samples formed close to the vents (Kuhn et al., 1998; Mills et al., 2001; Bau et al., 2014). Excess of Ce could ultimately be used as a proxy for the deposition rate and seawater exposure age of hydrothermal Fe-Mn deposits (Bau et al., 2014). Yttrium can also be used for distinguishing between hydrothermal, hydrogenetic and diagenetic Fe-Mn deposits. $Y_N/Ho_N$ ratios (normalized to PAAS) < 1 are the result of preferential scavenging of Ho compared to Y on Fe-Mn oxyhydroxide surfaces which produces a negative Y anomaly in hydrogenetic Fe-Mn deposits (Bau et al., 2014). Finally, the $Sm_N/Yb_N$ ratio shows the slope of the REE pattern. Unless there is a change in the REE sources in seawater, the slope of the REE pattern should not change. Therefore, one can use this ratio to identify a change in the REE sources in seawater.

Our sample set forms a continuum from actively forming Fe-Mn deposits formed through diffuse venting (Lau Basin, Lo'ihi seamount), and which have seen the influence from near-field hydrothermal inputs (deposits near the hydrothermal site); hydrogenetic Fe-Mn deposits formed on ridge flank and having recognized hydrothermal contribution (Bauer Basin), that we also define as far-field hydrothermal contribution (deposits located hundreds of kilometers from the vent source); and pure hydrogenetic Fe-Mn deposits from different oceanic regions.

## 2. Geological setting and sample description

### *2.1. Bauer Basin Fe-Mn deposits, Southeastern Pacific*

One hydrogenetic Fe-Mn crust sample and two diagenetic nodules from the Bauer Basin (BB) collected during the YALOC-73 cruise on the R/V Yaquina (Oregon State

University) at latitude 13°40'S and longitude 102°8'W (Lyle et al., 1977; Elderfield and Greaves, 1981) were selected (supplementary table S1). Bauer Basin is located in the South Pacific Ocean between the East Pacific Rise and Galapagos Rise (Heath and Dymond, 1977) and is therefore surrounded by active oceanic ridges. The two nodules were affected by diagenetic processes (Elderfield and Greaves, 1981) and the Fe-Mn crust was formed by hydrogenetic processes (Lyle et al., 1977). Previous studies have demonstrated that Fe-Mn oxide deposits including Fe-Mn crusts from the BB are prone to significant influence from hydrothermal inputs exported by seawater circulation through the ridge crests (Dymond and Veeh, 1975; Heath and Dymond, 1977; Lyle et al., 1977; Elderfield and Greaves, 1981). High metal/aluminium ratios found in sediments from the Bauer Basin and the negative Ce anomaly observed in Bauer Basin nodules is interpreted as being related to the transport of hydrothermal particles to the Bauer Basin (e.g., Fe-oxyhydroxides phases for rare earth elements) from hydrothermal sites located on the East Pacific Rise (EPR).

*2.2. Hydrothermal Fe-Mn oxide deposits from the Lau Basin, Southwestern Pacific*

Fe-Mn oxide deposits samples were collected in the southern back-arc Lau Basin (LB) during the NAUTILAU cruise on the R/V Nadir (Ifremer-Genavir) in April-May 1989 using the submersible Nautile (Figure 1 and supplementary table S1). The Valu Fa Ridge in the Lau Basin is an active back-arc spreading center where diffuse hydrothermal venting allows the deposition of Fe- and Mn-rich deposits (Fouquet et al., 1991). Fe-Mn-rich deposits were observed in both inactive and active hydrothermal vent fields including the Hine Hina site on the Southern Valu Fa Ridge, Vai Lili on the Central Valu Fa Ridge, and White Church on the Northern Valu Fa segment (Fouquet et al., 1993). Two samples were selected for our study: (1) NL-20-05, a 5 cm thick manganese crust collected at 1650 m water depth at the Vai Lili

223 site (Central Valu Fa Ridge), (2) NL-10-09, collected at 1908 m water depth at the White
224 Church site (Northern Valu Fa Ridge) and they consist of pieces of small inactive chimneys
225 composed of porous Mn-oxides (Fouquet et al., 1993). Hydrothermal fluids in this area have
226 higher metal concentrations and are notably enriched in Zn, As, Pb, Cd, Mn compared to mid-
227 ocean ridge vent fluids (e.g.; Fouquet et al., 1993; Mottl et al., 2011).
228
229 *2.3. Fe- and Mn-rich microbial mats at Lo'ihi seamount, Northern Pacific*
230
231 Hydrothermal Fe oxide deposits variably enriched in Mn were collected at both the
232 summit and the base of Lo'ihi seamount during three oceanographic cruises: FeMO 2006 on
233 R/V Melville (Scripps Institution of Oceanography) in October-November 2006, FeMO 2008
234 on R/V Thompson (University of Washington) in September-October 2008 and FeMO 2009
235 on the R/V Kilo Moana (University of Hawaii) in October 2009 using ROV Jason II (Woods
236 Hole Oceanographic Institution) (Figure 1). Details of sample collection can be found in
237 Glazer and Rouxel (2009), Edwards et al. (2011), (Rouxel et al., 2018).
238 Continuous diffuse venting of low temperature (0-60°C) hydrothermal fluids enriched
239 in Fe and depleted in $H_2S$ in comparison to mid-ocean ridge hydrothermal sources (Sedwick
240 et al., 1992; Wheat et al., 2000) allows thriving of abundant Fe-oxidizing bacteria that formed
241 massive biogenic Fe-rich mats observed at both the summit and base of Lo'ihi seamount
242 (Emerson and Moyer, 2002; Glazer and Rouxel, 2009; Edwards et al., 2011; Toner et al.,
243 2012; Rouxel et al., 2018). In particular, the ultra-diffuse hydrothermal venting at Ula Nui site
244 at the base of Lo'ihi seamount (~5000 m depth) produce extensive Fe-rich deposits (referred
245 as FeMO Deep mats) which are overlaid by a thin Fe-Mn crust (Edwards et al., 2011). Lo'ihi
246 Fe-Mn oxide deposits are considered to be actively forming and represent an ideal example of
247 low-temperature hydrothermal deposits.

### *2.5. Atlantic and Pacific hydrogenetic Fe-Mn crusts*

Bulk hydrogenetic Fe-Mn crusts from the Pacific Ocean were collected on Apuupuu seamount ~50 km south of Hawaii during FeMO 2009 cruise on the R/V Kilo Moana in October 2009 (supplementary table S1). These crusts were collected by ROV Jason II, and two of these Fe-Mn crusts were already investigated in Gueguen et al. (2016). Eight samples were selected for our study between 2000 and 3000 m depth. Fe-Mn crusts from the Atlantic Ocean were collected on the Ascension Fracture Zone (FZ), Vema FZ, Gloria FZ and the Azores Triple Junction (TJ) by dredging during two CNEXO cruises on the R/V Jean Charcot (cruises GIBRACO CH30 in August-September 1972 and BIOVEMA CH78 in October 1977) (Table 1 and Figure 1). Some subsamples of those crusts were prepared at the University of Cambridge (H. Elderfield and M. Greaves, pers. comm.).

Continuous discrete layers for each crust were not specifically sampled, but instead, we targeted Fe-Mn crusts from different oceanic regions of the globe. For each Fe-Mn crust sample we selected a subsample that was generally collected in depth of the crust, and does not correspond to surface scrapings. Instead, they correspond to relatively large sections, i.e. several millimeters to centimeters, of the crust. Accordingly, we refer our samples as “bulk crusts. ” They probably span a longer period of time than samples collected from discrete layers, and thus, each sample represents a range of ages, rather than a single point in time. No chronological information is expected to be obtained from this sample set. The subset of samples from Apuupuu seamount were previously dated and show a maximum age of 17.0 Ma with an average growth rate of 1.6 mm/Ma (Gueguen et al., 2016).

## **3. Methods**

### *3.1. Mineralogy*

The mineralogy of Fe-Mn deposits was determined by X-ray diffraction (XRD) Brucker AXS D8 Advance and Brucker AXS D2 Phaser at Ifremer (Brest, France) on bulk powder for hydrogenetic Fe-Mn crusts, Bauer Basin Fe-Mn deposits and Lau Basin Fe-Mn deposits. Dried powdered samples were deposited on a XRD sample holder and flattened with a glass slide. Samples were analyzed using Cu-Kα radiation over 2θ ranging from 2° to 70° at 40 kV and 30 mA. The mineralogy was assessed using Eva search-match software.

### *3.2. Major and trace elements composition*

Major, trace and rare earth element (REE) concentrations were measured by ICP-MS-Quadrupole (X-Series 2, Thermofisher Scientific) at the PSO (Pôle de Spectrométrie Océan), with the exception of Lo'ihi samples which were measured by ActLabs (Activation Labs, Canada) (Edwards et al., 2011). Hydrogenetic Fe-Mn crusts and Lau Basin samples were dissolved in $HNO_3$-HCl acid mixture and nodules and Lo'ihi Fe-rich deposits in an $HNO_3$-HCl-HF acid mixture. After evaporation residues were dissolved in 6M HCl as stock solutions. A fraction of the solution was diluted for ICP-MS analysis, and geological reference materials (GRMs) of Mn-nodules Nod-A-1 and Nod-P-1 were systematically run during each analytical session altogether with the samples. Concentrations were calibrated using a multi-elemental solution. Typical error obtained for all elements is generally better than 5% based on replicate measurements of geological reference materials. Results are presented in Table 1.

REE patterns were normalized to Post-Archean Australian Shale, the Ce anomaly is defined as $Ce/Ce^* = Ce_N/(Pr_N^2/Nd_N)$ (Lawrence et al., 2006) and the Y anomaly corresponds

298 to the ratio $Y_N/Ho_N$ (Bau et al., 2014), where subscript N stands for normalized values to
299 PAAS (Post-Archean Australian Shale; Taylor and McLennan, 1995).
300
301 *3.3. Ni isotope measurements*
302
303 Nickel isotopes were measured by MC-ICP-MS (Neptune, Thermofisher Scientific) at
304 the PSO (Pôle de Spectrométrie Océan) at Ifremer (Brest, France) (Table 1). Detailed
305 descriptions of the analytical methods can be found in (Gueguen et al., 2013), though a brief
306 description of methodology is provided below. After a two-stage purification method through
307 ion-exchange chromatography columns using AG1-X8 (for separating Fe, Zn and most of Co
308 and Cu) and Ni-spec Eichrom resins (for complete removal of remaining element matrix),
309 $^{60}Ni/^{58}Ni$, $^{61}Ni/^{58}Ni$, and $^{62}Ni/^{58}Ni$ ratios were measured by MC-ICP-MS in medium or high-
310 mass resolution mode with an ApexQ (ESI, USA) desolvation introduction system.
311 Instrumental mass discrimination was corrected using a double-spike method. A mix
312 of $^{61}Ni$ and $^{62}Ni$ isotopes was added to each sample prior to second step of chemical
313 purification, data reduction is based on calculations from (Siebert et al., 2001). Because Ni is
314 not retained on the first column step (columns are filled with an anionic AG1-X8 resin), we
315 did not consider necessary to spike the samples prior to the first separation step. Potential Ni
316 isotope fractionation during columns procedure have already been evaluated in a previous
317 study (Gueguen et al., 2013), and spiking samples only prior to the second separation does not
318 introduce any bias in the Ni isotope composition of the samples and standards. Spiked
319 solution of the international isotopic standard of nickel NIST SRM 986 was routinely
320 analyzed during each analytical session in a similar manner as a sample-standard-bracketing
321 method, which allows monitoring of the reproducibility of each analytical session.
322 Experimental and analytical methods are described in (Gueguen et al., 2013).

323 $^{60}Ni/^{58}Ni$ ratios of samples are reported as a deviation from NIST SRM 986 standard isotope
324 composition following equation (1) in per mil:
325
326 $$\delta^{60/58}Ni = (R_{spl}/R_{NIST986} - 1) \times 1000 \quad (1)$$
327
328 Where $R_{spl}$ is the $^{60}Ni/^{58}Ni$ ratio of the sample and $R_{NIST986}$ the $^{60}Ni/^{58}Ni$ ratio of the NIST
329 SRM 986 isotopic standard. Typical measurement precision achieved on Ni isotope ratios of
330 samples is better than ±0.04 ‰ (calculated with the replicate measurements of NIST SRM
331 986) and external precision (two-standard deviation) for delta measurements calculated from
332 replicate measurements of USGS (United States Geological Survey) Mn-nodules
333 geostandards Nod-A-1 and Nod-P-1 is better than ~ ±0.05 ‰. Replicates include analyses of
334 repeated digestion of geostandards subsamples, repeated processing of subsamples through
335 columns for Ni separation from the matrix, and repeated runs of samples on the mass
336 spectrometer.
337
338 **4. Results**
339 *4.1. Mineralogy*
340 Results of the mineralogy are shown in the supplementary data of Table S1. The
341 mineralogy of hydrogenetic Fe-Mn crusts is difficult to obtain because they are composed of
342 poorly crystallized phases. Our results indicate that hydrogenetic Fe-Mn crusts are composed
343 of a 10 Å Mn-phase, which could be todorokite, and then birnessite. Accessory phases such as
344 quartz, calcite and fluorapatite were encountered. The samples do not present traces of
345 phosphatization (only accessory phases like calcite and fluorapatite are present).
346 Ferromanganese deposits from the Bauer Basin and the Lau Basin are also composed
347 of todorokite (or a 10 Å Mn-phase) and then birnessite. However, these two deposits show

348 that mineral phases (based on the shape of the peak) were more crystallized than hydrogenetic
349 Fe-Mn crusts from this study. Sample NL-10-09 from the Lau basin is mainly constituted by
350 birnessite and then todorokite.
351 The mineralogy of Lo'ihi samples was published in previous studies (Edwards et al.,
352 2011; Toner et al., 2012), and indicate the presence of ferrihydrite and triclinic birnessite.
353
354 *4.2. Bulk hydrogenetic ferromanganese crusts from the Atlantic and Pacific oceans*
355
356 Fe/Mn ratios are generally higher for Atlantic samples, i.e., Ascension FZ, VEMA FZ
357 and Gloria FZ, with values ranging from 1.27 to 1.87 and in the range of the average Fe/Mn
358 ratio for Atlantic crusts (i.e., 1.44; Hein et al., 2013) compared to Pacific crusts (Apuupuu
359 seamount) with Fe/Mn ratios ranging from 0.65 to 1.17 consistent with average Fe/Mn ratio
360 of the Pacific Prime crust zone (i.e., 0.74; Hein et al., 2013). Fe/Mn ratios in the Azores TJ
361 crusts are an exception because they have Fe/Mn ratios as low as 0.39. We observed that the
362 lowest Fe/Mn ratios are found for crusts recovered at shallower depths (i.e., Apuupuu and
363 Azores TJ Fe-Mn crusts). There is a significant compositional variability in the sample set.
364 Notably, the concentration of Ni is up to two times higher in Azores TJ crusts (up to 5,495
365 µg/g) than in other Fe-Mn crusts from the Atlantic (average of 2581 ppm; Hein et al., 2013).
366 Co is also four times more enriched in Azores TJ crusts (up to 12,549 µg/g) compared to the
367 average of 3,608 µg/g in Atlantic crusts (Hein et al., 2013). Azores TJ crusts exhibit the
368 highest Ni/Mn (0.023 and 0.022) and Co/Mn ratios (0.047 and 0.054) compared to other Fe-
369 Mn crusts (i.e., between 0.009 and 0.017, and between 0.016 and 0.039 respectively). On the
370 other hand, Azores TJ samples have the lowest Zn/Mn ratios (~0.024) compared to other Fe-
371 Mn crusts (Zn/Mn between 0.0025 and 0.0044 but with most values > 0.0030) (Figure 3).
372 They also have the lowest Cu/Mn ratios (<0.0030), while Fe-Mn crsuts from Apuupuu,

Ascension FZ, VEMA FZ and Gloria FZ have values between 0.0047 and 0.0075 (with the exception of two samples with Cu/Mn ratios of 0.0012 and 0.0028).

Rare earth elements patterns normalized to PAAS display a positive Ce anomaly and a negative Y anomaly typical of hydrogenetic deposits (e.g., Bau et al., 1996) (Figure 2). Results show that REE are depleted in Apuupuu and Azores TJ samples compared to other Fe-Mn crusts from the study, and that the Y anomaly is less pronounced. All Fe-Mn crusts samples plot in the hydrogenetic field in the Ce/Ce* vs. $Y_N/Ho_N$ diagram (Figure 2).

$\delta^{60/58}$Ni values for the hydrogenetic Fe-Mn crusts range from 0.8 ‰ to 1.8 ‰ with most values clustering between 1.3 and 1.6 ‰ (Table 1 and Figure 5B). Azores TJ Fe-Mn crusts show distinct elemental composition (e.g., higher Co/Mn and Ni/Mn and lower Fe/Mn) compared to other Atlantic Fe-Mn crusts but have similar $\delta^{60/58}$Ni values (Figure 4). On the other hand, variable $\delta^{60/58}$Ni values among Gloria FZ, VEMA FZ and Ascension FZ Fe-Mn crusts are not associated with significant variations in elemental concentrations (Figures 3 and 4). Nickel isotope compositions of hydrogenetic Fe-Mn deposits reported here overlap with the range of $\delta^{60/58}$Ni values reported in the literature. Gueguen et al. (2016) reported an average $\delta^{60/58}$Ni value of 1.79 ±0.21 ‰ for subsamples collected along stratigraphic profiles acquired in two North Pacific Fe-Mn crusts (Hawaii archipelago) similar to the average value of 1.73 ±0.21 ‰ obtained for two South Pacific Fe-Mn crusts (Tahiti Archipelago). Gall et al. (2013) reported a range of $\delta^{60/58}$Ni values between 0.9 ‰ and 2.5 ‰ for Fe-Mn crusts collected in various oceanic regions, yielding a best estimate for Fe-Mn crusts of 1.6 ‰ (Figure 5). We could not confirm the initial observations made by Gall et al. (2013) that Ni isotope compositions in Fe-Mn crusts vary in relation to their distance to continental shelf (Figure 5). In contrast, Ni isotope composition tends to correlate with water depth and shallowest crusts exhibit the lowest Fe/Mn ratios and the heaviest $\delta^{60/58}$Ni value (Figure 5).

398 *4.3. Ferromanganese oxide deposits from the Bauer Basin, Southwest Pacific*

399

400 Fe/Mn ratios in BB nodules (0.20 and 0.44) are lower than in BB Fe-Mn crust (0.98),
401 the latter being in the range of hydrogenetic Fe-Mn crusts from Apuupuu and the Atlantic.
402 Nickel concentration in BB Fe-Mn crust of 5,886 µg/g is about twice the average of Apuupuu
403 Fe-Mn crusts average value of 2,262 µg/g but it is closer to the average of the North Pacific
404 Prime Zone of 4,216 µg/g (Hein et al., 2013). Nickel contents in BB Mn-nodules are 11,850
405 µg/g and 10,054 µg/g which are close to the average Ni concentration of 13,002 µg/g for
406 nodules from the Clarion Clipperton Fault Zone (CCFZ) in the Central Pacific (Hein et al.,
407 2013). BB nodules and crust have higher Ni/Mn ratios (between 0.03 and 0.05), Zn/Mn ratios
408 (between 0.0046 and 0.0060) and Cu/Mn ratios (0.015 to 0.020) relative to Fe-Mn crusts
409 (Ni/Mn<0.02, Zn/Mn <0.0044 and Cu/Mn<0.0075). In contrast, Co/Mn ratios for the three
410 BB samples are lower (between 0.002 and 0.005) compared to hydrogenetic Fe-Mn crusts
411 (>0.0016). Rare earth elements patterns of BB Fe-Mn deposits are enriched in REE relative to
412 PAAS (Figure 2), they show a negative Ce anomaly and the Y anomaly is not observed, as
413 reported in previous studies (Elderfield and Greaves, 1981; Elderfield et al., 1981b; Elderfield
414 et al., 1981a). In the Ce/Ce* vs. $Y_N/Ho_N$ diagram (Figure 2), BB nodules fall in the diagenetic
415 field and the BB crust in the hydrothermal field.

416 $\delta^{60/58}$Ni values of the BB Fe-Mn crust of 0.33 ‰, and of 0.42 ‰ and 0.43 ‰ for BB
417 nodules stand in marked contrast compared to heavier $\delta^{60/58}$Ni values (averaging ~1.6 ‰)
418 reported for hydrogenetic crusts and nodules of this study and previously reported values by
419 Gall et al. (2013) and Gueguen et al. (2016) (Table 1).

420

421 *4.4. Hydrothermal Fe-Mn oxide deposits from the Lau Basin, Southeast Pacific*

422

Fe-Mn oxide deposits from the Lau Basin are essentially composed of birnessite Mn-oxides phases, which is reflected in the very low Fe/Mn ratios < 0.002. Ni/Mn, Co/Mn, Zn/Mn and Cu/Mn ratios (<0.0003; <0.00009; <0.0009; and <0.0012, respectively) are also extremely low compared to hydrogenetic Fe-Mn crusts and Bauer Basin deposits. Rare earth elements patterns normalized to PAAS for both samples exhibit a negative Ce anomaly, a positive Eu anomaly and a positive Y anomaly. The negative Ce anomaly and positive Eu anomaly are more pronounced for NL-20-05 than for NL-10-09, but the positive Y anomalies have the same amplitude. The overall REE patterns indicate that Lau Basin hydrothermal deposits are depleted in REE relative to hydrogenetic Fe-Mn crusts of this study by 2 to 3 orders of magnitude but instead have the same level of enrichment as hydrothermal Fe-Mn deposits from Lo'ihi (Figure 2). LB Fe-Mn deposits fall in the hydrothermal field in the Ce/Ce* vs. $Y_N/Ho_N$ diagram. These samples display $\delta^{60/58}$Ni values of 0.51 and 1.11 ‰ for NL-10-09 and NL-20-05 respectively (Table 1). These values are lighter than the average range of value (1.3 - 1.6 ‰) reported for hydrogenetic Fe-Mn crusts from this study and from the literature (Gall et al., 2013; Gueguen et al., 2016).

*4.5. Hydrothermal Fe-Mn oxide deposits from Lo'ihi seamount, North Pacific*

Mineralogy of the deposits is essentially composed of ferrihydrite and triclinic birnessite (Edwards et al., 2011; Toner et al., 2012), and samples are characterized by high Fe/Mn ratios (between 2.84 and 16.68) and low metal/Mn ratios (i.e., Co/Mn ~ <0.003; Cu/Mn ~ <0.003; Zn/Mn ~ <0.003; and Ni/Mn ~ <0.008) compared to other Fe-Mn deposits described in this study (Figure 3). Geochemical composition of Lo'ihi Fe-Mn oxides is reported in (Table 1). REE patterns normalized to PAAS for Lo'ihi deposits show that the REE content is depleted relative to hydrogenetic Fe-Mn crusts and show flat patterns with a

small positive Eu anomaly (Figure 2). The Ce/Ce* vs. $Y_N/Ho_N$ diagram shows that Lo'ihi samples are in the hydrothermal field (Figure 2).

$\delta^{60/58}$Ni values range from -1.49 to -0.80 ‰: with the exception of one sample (J2-244-SS5), heaviest $\delta^{60/58}$Ni values are associated with highest Ni/Mn and Fe/Mn ratios (Figure 4). The absence of correlation between $\delta^{60/58}$Ni values and Al/Fe ratios rules out the influence of detrital particles like volcanic debris in Fe-rich mats on Ni isotopes.

## 5. Discussion

### *5.1. Mechanisms of Ni isotope fractionation and formation of marine ferromanganese deposits*

Consistent with previous studies (Gall et al., 2013; Gueguen et al., 2016), hydrogenetic crusts are characterized by isotopically heavy, yet variable, Ni isotope signatures ($\delta^{60/58}$Ni values range from 0.9 ‰ and 2.5 ‰). Our results suggest that Ni isotope composition of Fe-Mn crusts, may be fractionated towards both lighter to heavier values relative to modern deep seawater (average ~1.4 ‰). Hydrogenetic Fe-Mn crusts are formed by slow precipitation of Fe-Mn colloids from seawater, with the volcanic substrates of seamounts allowing the precipitation of Fe-Mn oxyhydroxides (Koschinsky and Halbach, 1995; Koschinsky and Hein, 2003; Koschinsky et al., 2003). The process of Mn oxidation at the base of the Oxygen Minimum Zone (OMZ) provides an efficient scavenging process of seawater dissolved trace metals, such as Co, Ni, Zn, Tl and Cd, by Mn-oxide colloids, which contributes to precipitation of Mn-rich layers of Fe-Mn crusts (e.g.; Mizell et al., 2020). Several mechanisms may, therefore, contribute to the variability of Ni isotope composition in Fe-Mn crusts, and we explore them below.

473 *5.1.1. The role of Ni speciation in seawater and in the water column*

474

475 The water depth and local oceanographic setting are potentially important parameters
476 affecting the chemical composition of Fe-Mn crusts. Results from Fe-Mn crusts from the Line
477 Islands (Aplin and Cronan, 1985), the Hawaii chain (De Carlo et al., 1987) and the Central
478 Pacific (Halbach et al., 1984) indicate that crusts formed in shallow waters can have four
479 times lower Fe/Mn ratios and up to ten times higher metal concentrations (Ni, Co, V, Pb, Mo,
480 Cd) than deeper crusts. In deeper waters (> 3000 m depth), Fe-Mn crusts are generally
481 characterized by higher Fe/Mn ratios due to lower inputs of Mn from the OMZ in addition to
482 an increased Fe flux through the dissolution of carbonate testas from microorganisms below
483 the CCD (Halbach and Puteanus, 1984). Other factors such as, increase of the pH favoring
484 precipitation of Fe, increase of the detrital particles in the water column (Mizell et al., 2020),
485 and input of Fe from deep hydrothermal sources (Horner et al., 2015), may explain increasing
486 Fe/Mn ratios in crusts with depth. By contrast, in shallow waters, e.g., below the OMZ (i.e.,
487 located between 500 m and 1500 m depth), the proportion of Mn-rich colloids in the water
488 column is presumably high (e.g.; Klinkhammer and Bender, 1980). The lowest Fe/Mn ratios
489 in our sample set correspond to shallowest (< 2500 m water depth) hydrogenetic Fe-Mn crusts
490 associated with the heaviest $\delta^{60/58}$Ni values (i.e., > 1.5 ‰) (Apuupuu and Azores TJ, Figures 4
491 and 5). Azores TJ samples have the highest Co/Mn ratios (~0.5), while Apuupuu crusts have
492 ratios in the range of other crust of the study (0.2-0.3). Hydrogenetic Fe-Mn crusts from
493 Gloria, Ascension and VEMA areas collected at water depth > 2500 m have the lightest
494 $\delta^{60/58}$Ni values (between 1.5 ‰ and 0.8 ‰) and the highest Fe/Mn ratios. More than 90% of
495 the Ni in Fe-Mn nodules and crusts is in the Mn-phase (Koschinsky and Halbach, 1995;
496 Mohwinkel et al., 2014; Wegorzewski et al., 2020), and this phase association does not
497 change with water depth. As a consequence, a change in the Fe/Mn ratio in the crusts should

not impact the Ni isotope composition of the crusts. In addition, the variability of Ni isotope composition in deep water (i.e., < 1500 m water depth) is very limited < 0.2 ‰, while surface waters (< 200 m water depth) deviate by 0.4 to 0.5 ‰ relative to deep water (Cameron and Vance, 2014; Takano et al., 2017; Wang et al., 2019; Archer et al., 2020). Therefore, it is unlikely that variations in Fe-Mn crusts are explained by the variability of Ni isotopes in oceanic water masses.

An alternative explanation, but not mutually exclusive, is to consider isotopic fractionation between inorganic and organic ligands. Experimental and theoretical studies on Ni isotopes demonstrate fractionations up to 2.5 ‰ for $\delta^{60/58}$Ni values during exchange reactions between inorganic and organic ligands, with a range of fractionation of ~1.7 ‰ between inorganic species and a range of 2.5 ‰ between organic species (Fujii et al., 2011). Accordingly, if one of these fractionated species is preferentially adsorbed onto the oxyhydroxide surface it would impart a net isotope fractionation between the mineral and the solution. In addition, hydrated $Ni^{2+}$ ions are isotopically heavier than Ni-chloro complexes in the order of $Ni^{2+} > NiCl^{+} > NiCl_2$ (Fujii et al., 2011). Therefore, one could speculate that aqueous $Ni^{2+}$, which is presumably preferentially adsorbed onto Fe-Mn crusts (Koschinsky and Halbach, 1995), would be enriched in heavy Ni isotopes relative to other inorganic species and organic species, thus consistent with heavier Ni isotopes in hydrogenetic Fe-Mn crusts relative to Ni isotopes in seawater.

*5.1.2. Isotopic fractionation during Ni sorption processes*

It has been well documented that Ni is bound to Mn-oxyhydroxides and is easily adsorbed onto these phases (Hem, 1978; Koschinsky and Halbach, 1995; Koschinsky and Hein, 2003; Peacock and Sherman, 2007a; Peacock and Sherman, 2007b), and that Ni

adsorbed on birnessite is structurally incorporated within the mineral structure with time (Peacock, 2009). Recent results for Ni sorption on birnessite indicate large Ni isotope fractionation up to ~ -3 ‰ on the solid phase because structural vacancies in birnessite are preferentially occupied by light Ni isotopes (Sorensen et al., 2020). The composition of hydrogenetic Fe-Mn crusts enriched in heavier Ni isotopes compared to seawater is therefore, at odds with experimental data. However, Gueguen et al. (2016) showed that light $\delta^{60/58}$Ni values up to 0.25 ‰ in hydrogenetic Fe-Mn crusts from the South Pacific were the result of post-depositional and alteration processes at the bottom of the crust in contact with the substrate. They proposed that circulating fluids altered the substrate at the bottom of the hydrogenetic crusts which result in dissolution and reprecipitation of Mn-oxyhydroxide phases. This was accompanied by Ni isotope fractionation during sorption to Mn-oxyhydroxide phases producing anomalously light $\delta^{60/58}$Ni values. Consistent with these results, light $\delta^{60/58}$Ni values (-0.8 ‰ to -0.2 ‰) found in metalliferous sediments are interpreted as the result of diagenetic processes affecting the Ni cycling with Mn under oxic conditions (Little et al., 2020). Therefore, significant isotope fractionation during Ni sorption and the importance of alteration and deposition processes highlight the importance of mineralogy and formation processes for Ni isotope fractionation in marine Fe-Mn deposits.

Despite the poor crystallinity of our hydrogenetic Fe-Mn crusts samples, we could identify two predominant Mn- phases (with the exception of Lo'ihi deposits mainly constituted by Fe- phases) : a 10 Å Mn-phase (maybe todorokite) and then birnessite. By contrast, LB deposits are predominantly composed of birnessite and to a lesser extent todorokite and they have lighter $\delta^{60/58}$Ni values (0.5 and 1.1 ‰) than hydrogenetic Fe-Mn crusts. Identification of the mineral phases is easier for these samples due to their greater crystallinity in comparison to hydrogenetic Fe-Mn crusts. Little et al. (2020) hypothesized that light $\delta^{60/58}$Ni values from -0.8 ‰ to -0.2 ‰ in metalliferous sediments from two MANOP

548 (Manganese Nodule Project) sites are related to post-depositional processes involving the
549 dissolution and reprecipitation of Mn-oxides during diagenesis (Little et al., 2020). The
550 authors propose that the diagenetic cycling of Ni associated with Mn could be a key process
551 for explaining light Ni $\delta^{60/58}$Ni values in marine metalliferous deposits. For example, they
552 suggest that the transformation of birnessite to todorokite under oxic conditions could favor
553 the preferential incorporation of Ni in todorokite. Therefore, if we compare these results with
554 results from our study, a mineralogical change in the Mn-phase in deeper hydrogenetic Fe-Mn
555 crusts could possibly explain the lighter Ni isotope values in hydrogenetic Fe-Mn crusts
556 (Gloria, Ascension and VEMA) compared to Azores TJ and Apuupuu Fe-Mn crusts; although
557 we agree that more in-depth mineralogical analyses are necessary to confirm this assumption.
558 On the other hand, this interpretation is not consistent with our results for the Lau Basin,
559 because the lighter $\delta^{60/58}$Ni value (0.5 ‰) observed in sample NL-10-09 has a predominance
560 of birnessite, while the sample NL-20-05 with a $\delta^{60/58}$Ni value of 1.1 ‰ is predominantly
561 composed of todorokite. This implies that the mineralogy of Lau Basin is probably not the
562 cause for the difference in $\delta^{60/58}$Ni values between the two samples.
563
564 *5.1.3. Are hydrothermal sources of Ni recorded in Fe-Mn deposits ?*
565
566 Before the discovery of active hydrothermal sources, low Al/(Al+Fe+Mn) ratios found
567 in deep-sea sediments from the East Pacific were interpreted as being linked to inputs from
568 the volcanic activity of the East Pacific Rise (Boström et al., 1969). This suggests that Fe-Mn
569 precipitates can travel over thousands of kilometers away from the vents. Recent evidence
570 from direct measurements of seawater during the GEOTRACES transects, shows that Fe and
571 Mn emitted at the EPR are transported several hundreds of kilometers away from the vents
572 (e.g.; Lam et al., 2018; Lee et al., 2018). The transport of Ni is not as well documented as for

Fe and Mn. However, results of the Ni concentration in seawater above a hydrothermal source measured along the GEOTRACES transect GP16 in the South East Pacific, shows that the background Ni concentration in seawater is not perturbed (Lee et al., 2018).

Nickel concentrations in hydrothermal fluids are generally close to seawater due to negligible mobilization of Ni during alteration of the oceanic crust (Von Damm, 1995). Differences are, nevertheless, observed depending on geological settings, i.e., Ni concentrations of 2-3 µmol/L were measured in Rainbow vent fluids on the mid-Atlantic oceanic ridge (Douville et al., 2002), in comparison to the range of values for dissolved Ni in deep seawater of 6-10 nmol/L and surface seawater of 2-5 nmol/L (Cameron and Vance, 2014; Takano et al., 2017; Wang et al., 2019; Archer et al., 2020). Because ultramafic-hosted hydrothermal vents are not the predominant type of hydrothermal systems, the global Ni hydrothermal flux to the oceans is presumably low, implying that high-temperature hydrothermal fluids are probably not a major contributor to the Ni oceanic budget. However, significant Ni enrichment has been observed in low-temperature hydrothermal venting (Sedwick et al., 1992; Wheat et al., 2002; Wheat et al., 2003), which could possibly produce a significant flux of Ni to the oceans.

Marine Fe-Mn deposits represent one possible way to investigate the effect of direct contribution of hydrothermal sources on the Ni oceanic budget and Ni isotopes in seawater through time. For example, several studies demonstrated that the geochemistry of Fe-Mn crusts could be affected by hydrothermal inputs from distal (far-field) hydrothermal sources (Elderfield and Greaves, 1981; van de Flierdt et al., 2004; Chu et al., 2006; Gall et al., 2013). More specifically for Ni, Gall et al. (2013) attributed the range of Ni isotope values in Fe-Mn crusts from 0.9 to 2.5 ‰ to variable Ni sources in seawater, in particular hydrothermal sources, where lighter $\delta^{60/58}$Ni values in a Central Pacific Fe-Mn crust were tentatively ascribed to local hydrothermal inputs in the water column (Gall et al., 2013). Little et al.

598 (2020) considered that Ni scavenging onto hydrothermal Fe particles followed by their
599 deposition in the sediment, is one of the possible explanations for light Ni isotopes (up to ~ -
600 0.8 ‰) observed in metalliferous sediments from the MANOP site M close to the East Pacific
601 Rise. Therefore, hydrothermal inputs are a possible factor for explaining the variability of Ni
602 isotopes in Fe-Mn deposits, and thus a key process for estimating the Ni isotope composition
603 of the oxic Mn sink. In the following section, we intend to address this hypothesis by
604 investigating hydrothermal and mixed hydrothermal-hydrogenetic deposits using the
605 combination of rare earth element systematics and Ni isotopes.
606
607 *5.2. A classification scheme using REE and Ni isotopes*
608
609 The combination of REE geochemistry and Ni isotopes could give us insights for
610 deciphering Ni sources and formation processes in a continuum of well-characterized
611 hydrogenetic Fe-Mn crusts, hydrothermal deposits (Lo'ihi and Lau basin), and hydrogenetic
612 Fe-Mn deposits with a contribution from far-field hydrothermal inputs (i.e., Bauer basin). We
613 use three indicators in our study: Ce anomaly, Y anomaly and $Sm_N/Yb_N$ ratio. A positive Ce
614 anomaly is an indicator of excess of accumulation of Ce in hydrogenetic Fe-Mn cruts due to
615 oxidation of Ce(III) to Ce(IV) at the surface of Fe-Mn crusts (Bau et al., 2014). By contrast,
616 hydrogenetic Fe-Mn crusts are characterized by a negative Y anomaly ($Y_N/Ho_N$ ratio < 1), and
617 indicates preferential scavenging of Ho rather than Y on its surface. Finally, the $Sm_N/Yb_N$
618 ratio is an indicator of the variation of the slope in the REE pattern, and this would potentially
619 indicate changes in the REE source to the deposits. Our samples are classified according to
620 Figure 6: the hydrogenetic field (i.e., Fe-Mn crusts) is defined for Fe-Mn deposits with
621 $\delta^{60/58}$Ni values > 0 ‰, Ce/Ce* > 1, $Y_N/Ho_N$ < 1 and $Sm_N/Yb_N$ < 0.6; the hydrothermal field
622 (i.e., Lo'ihi deposits) is defined by $\delta^{60/58}$Ni values < 0‰, Ce/Ce* < 1, $Y_N/Ho_N$ > 1 and

623 $Sm_N/Yb_N$ > 0.6; and the mixed hydrothermal-hydrogenetic field (i.e., LB deposits and BB
624 deposits) corresponds to $\delta^{60/58}$Ni values > 0‰, Ce/Ce* < 1, $Y_N/Ho_N$ > 1 and $Sm_N/Yb_N$ > 0.6.
625 The threshold value of 0.6 for the $Sm_N/Yb_N$ ratio is defined based on the distribution of BB
626 deposits (Figure 6). Based on these observations, we discuss below the impact of a possible
627 influence of hydrothermal inputs in our selection of Fe-Mn deposits.
628
629 *5.2.1. Ferromanganese deposits formed near seafloor hydrothermal sources:*
630 *examples from the Lo'ihi seamount (North Pacific) and the Lau Basin (Western Pacific)*
631
632 Rare earth elements, Co/Mn ratios and Fe/Mn ratios of Lo'ihi and LB deposits indicate
633 a hydrothermal origin of these deposits, i.e., they are influenced by near-field hydrothermal
634 inputs. They represent two end-members, Fe-rich and Mn-rich respectively. REE-depleted
635 patterns of Lo'ihi and LB deposits show a positive Eu anomaly which is more pronounced in
636 the LB deposits. While the negative Ce anomaly and HREE enrichment in LB deposits are
637 typical of a seawater source for REE, the positive Eu anomaly is a robust signature of REE
638 derived from high temperature hydrothermal fluids (German et al., 1990). The Ce/Ce* vs.
639 $Y_N/Ho_N$ diagram does not discriminate between LB deposits and Loi'hi deposits. LB deposits
640 display different $\delta^{60/58}$Ni values compared to Lo'ihi deposits, i.e., positive $\delta^{60/58}$Ni values of
641 0.5 ‰ and 1.1 ‰ and negative $\delta^{60/58}$Ni values from -1.5 ‰ to -0.7 ‰, respectively. Thus,
642 although both Lo'ihi and LB deposits are affected by hydrothermal inputs, the fractionation of
643 Ni isotopes is clearly different between the two deposits, suggesting that the effects induced
644 by near-field hydrothermal inputs are different according to the type of deposits.
645 The combination of REE and Ni isotopes data presented in Figure 6 show that Lo'ihi
646 deposits systematically fall in the hydrothermal field, with negative $\delta^{60/58}$Ni values, negative
647 Ce anomalies, positive Y anomalies and $Sm_N/Yb_N$ ratios > 0.6. In contrast, as indicated by

$Sm_N/Yb_N$ ratios < 0.6 and $\delta^{60/58}$Ni values > 0 (Figure 6), LB deposits have probably a contribution from both a hydrothermal source and a hydrogenetic source. Three possible causes can explain the difference in Ni isotope composition between Lo'ihi and LB deposits, (1) growth rates, (2) $\delta^{60/58}$Ni value of the source fluid, and (3) mineralogy and processes of Ni removal from the fluid and/or from seawater. Growth rates could be different due to the geological context of the hydrothermal source (e.g., back-arc basin, slow versus fast spreading ridges) or composition of the hydrothermal fluids. But because both deposits formed close to hydrothermal venting, growth rates are likely of the same order. Additional measurements of the growth rates of LB and Lo'ihi deposits would confirm this statement, but they are likely different and faster in comparison to hydrogenetic crusts, which does not favor hypothesis 1.

Nickel concentrations up to 80 nmol/L have been measured in Lo'ihi hydrothermal fluids (Sedwick et al., 1992), which is about 10 times the average seawater concentration (Sclater et al., 1976; Bruland, 1980; Cameron and Vance, 2014; Takano et al., 2017; Wang et al., 2019). However, the Ni isotope composition of Lo'ihi hydrothermal fluids has not been published yet. Our best assumption is to consider that Ni isotopes in the fluid have either the composition of the basalt (i.e., ~BSE, 0.1 ‰), or the composition of seawater (i.e., ~1.4 ‰). LB deposits formed by low temperature diffuse hydrothermal venting through the volcanic substrate, and REE-depleted but HREE-enriched patterns and the negative Ce anomalies suggest that they formed by mixing between seawater and hydrothermal fluids. Therefore, we speculate that the Ni isotope composition of the source fluids in both Lo'ihi and LB deposits ranging between volcanic rock and seawater values (0 to 1.4 ‰), does not explain the most negative $\delta^{60/58}$Ni values from -1.5 ‰ to -0.7 ‰ at Lo'ihi. Hence, we do not favor hypothesis 2 implying variable Ni isotope composition of the sources.

Lo'ihi deposits are dominated by Fe-phases (i.e., Fe/Mn ratios range from 2.84 to 16.68), while LB deposits are dominated by Mn-phases (i.e., Fe/Mn ratios < 0.002). Thus, it is

673 possible that the mineralogy and processes involved in Ni removal in the deposits, influenced
674 the fractionation of Ni isotopes (hypothesis 3). Nickel isotope fractionation during sorption on
675 Fe- and Mn-oxide has been determined through experimental studies and it was shown that
676 the Fe-Mn mineral phase is systematically enriched in light Ni isotopes (Wasylenki et al.,
677 2015; Gueguen et al., 2018; Sorensen et al., 2020). The Ni isotope fractionation is much
678 larger on Mn-oxides than Fe-oxides (i.e., in the order of -2 ‰ to -3 ‰ for Mn-oxides, and -0.8
679 ‰ to -0.3 ‰ for Fe-oxides). Ni/Mn ratios are very low in LB deposits for two reasons. First,
680 LB deposits are composed of pure Mn-oxides (Fe is almost a trace element and Fe/Mn <
681 0.002). Second, Ni concentration is low (~10-12 nmol/L) in seawater and probably in the
682 hydrothermal fluid. This observation, combined with the fast rate of precipitation (e.g., low
683 Co/Mn ratios), did not allow scavenging of large amount of Ni in LB (in comparison with
684 hydrogenetic Fe-Mn crusts for example) as shown by relatively low Ni concentrations
685 (between ~50 $\mu g.g^{-1}$ and ~100 $\mu g.g^{-1}$) and Ni/Mn ratios <0.0003. Lighter $\delta^{60/58}$Ni values (0.5
686 ‰ and 1.1 ‰) in LB deposits compared to seawater values (~1.4 ‰) may reflect reservoir
687 and/or mineralogical effects through scavenging of seawater trace metals in hydrothermal
688 Mn-phases (i.e., birnessite and or todorokite; Fouquet et al., 1993). One can assume that after
689 formation of LB deposits by precipitation of metals from seawater and hydrothermal fluids,
690 subsequent aging of the deposits and exposure at the seafloor allows further scavenging of
691 seawater-derived elements including Ni on Mn-oxides phases. Such mechanism have been
692 suggested for Cd isotopes sorption to birnessite (Wasylenki et al., 2014), with slow exchange
693 of Cd between seawater and birnessite.
694 By contrast, isotopically light Ni (from -1.5 ‰ to -0.8 ‰) in Lo'ihi deposits is due to
695 the removal of Ni during Ni adsorption from seawater and from the hydrothermal fluid,
696 followed by isotope fractionation between the fluid and mixed Mn/Fe-oxides based on
697 experimental results of Ni sorption to Mn-oxides (Sorensen et al., 2020) and Fe-oxides

(Wasylenki et al., 2015; Gueguen et al., 2018). Our results can be compared to metalliferous deposits from the MANOP site M (East Pacific), which show light $\delta^{60/58}$Ni values up to -0.8 ‰ and a similar range of Fe/Mn ratios from 3.8 to 44.6 (most values are between 3.6 and 6.3) (Little et al., 2020) than Lo'ihi deposits (between 2.8 and 16.7). The results of Little et al. (2020) were interpreted as possibly being the result of the deposition of hydrothermal Fe oxyhydroxides associated with sorption of isotopically light Ni onto the hydrothermal Fe oxyhydroxides.

*5.2.2. Fe-Mn deposits affected by far-field hydrothermal activity: example from the Bauer Basin (Eastern Pacific)*

It has been proposed that oceanic circulation in the Bauer Basin allows export of hydrothermal precipitates from the East Pacific Rise (EPR) (Heath and Dymond, 1977; Lyle et al., 1977; Ravizza and McMurtry, 1993). Elderfield and Greaves (1981) suggested that diagenetic processes in the sediment allowed the incorporation of hydrothermal Fe-oxides and REE with negative Ce anomalies ($Ce/Ce^* < 0.5$) in the BB nodules, while the BB Fe-Mn crust has a hydrogenetic origin (Lyle et al., 1977). This is confirmed by the Ce/Ce* vs. $Y_N/Ho_N$ diagram (Figure 2) showing that the BB crust falls in the hydrothermal field, and the BB nodules in the diagenetic field. In addition to their negative Ce anomaly, REE patterns of BB samples (crust and nodules) are on average depleted compared to other hydrogenetic deposits (Table 1). Another important feature of the BB crust and nodules is their unusually low Co/Mn ratios (Co/Mn <0.005). Therefore, REE patterns and low Co/Mn ratios in BB deposits could indicate hydrothermal input of Fe-Mn from the EPR in the deposits, either during diagenetic reactions for the nodules, or by settling of hydrothermal plume fallouts during formation of Fe-Mn crusts. The latter process has been previously suggested for Fe-

Mn crusts from the Central Indian Ridge (Kuhn et al., 1998). Finally, the contribution from direct hydrothermal fluids in BB Fe-Mn oxide deposits can be precluded because the average Ni/Mn ratios in hydrothermal fluids from the global ocean (Von Damm, 1995; Douville et al., 2002) are much lower than Ni/Mn ratios in the BB Fe-Mn deposits. In addition, samples also do not have a positive Eu anomaly indicative of REE precipitation from high temperature hydrothermal fluids (the Bauer Basin is located ~1000 km to the East of the EPR).

$\delta^{60/58}$Ni values in BB crust and nodules, i.e., 0.3 ‰ and 0.4 ‰ respectively, are isotopically lighter than the average range for hydrogenetic Fe-Mn crusts of 1.3-1.6 ‰ (Figure 5B) and the average seawater of 1.4 ‰. The light $\delta^{60/58}$Ni values in BB nodules could possibly be explained by diagenetic remobilization of Ni within the sediment, as suggested by Little et al. (2020) for Mn-nodules and metalliferous sediments from the Eastern Pacific and in agreement with Elderfield and Greaves (1981) for rare earth elements in BB nodules. However, it is unlikely that the same process applies to the BB Fe-Mn crust. Accordingly, in agreement with the REE geochemistry, we favor the implication of far-field inputs from hydrothermal sources through dispersed hydrothermal plume fallouts, such as Fe-oxides precipitates which sorbed isotopically light Ni, on the formation of BB Fe-Mn crust and possibly Mn-nodules. Little et al. (2020) also proposed that light $\delta^{60/58}$Ni values up to -0.8 ‰ in metalliferous sediments deposited close to the East Pacific Rise could be due to scavenging of light Ni isotopes on hydrothermal Fe-oxides, which were then incorporated in the sediments. We suggest that a similar process could have occurred for BB Fe-Mn crust, whereby scavenging of isotopically light Ni onto either hydrothermal Mn- or Fe-oxides were then deposited in Fe-Mn crusts.

### *5.3. Nickel isotopes in marine Fe-Mn deposits and implication for the marine Ni isotope budget*

748

749 Investigation of rare earth elements and Ni isotopes in a continuum of marine Fe-Mn
750 deposits from typically hydrothermal, to various mixed hydrothermal and hydrogenetic and to
751 strictly hydrogenetic shows that Ni isotopes in Fe-Mn deposits are variable. These results
752 confirm that Fe-Mn crusts do not provide an accurate record of the global burial flux of Ni
753 and its isotopes via sorption to Fe-Mn oxides, implying that the Ni isotope composition of the
754 global sink of Ni Mn-oxides is not necessarily best represented by hydrogenetic Fe-Mn crusts.
755 Seafloor hydrothermal vents represent the main Mn source in seawater (Elderfield and
756 Schultz, 1996), producing widespread Mn enrichment, both in the water column and seafloor
757 sediments, up to 1000's km away from the spreading axis (e.g., Klinkhammer and Hudson,
758 1986; Resing et al., 2015). In particular, the relationship between dissolved Mn and $^{3}$He in the
759 plume off South EPR indicates that a large fraction of hydrothermal Mn is precipitated within
760 the vicinity of ridge axis, while a minor but still significant fraction behaves conservatively
761 and disperse away in the ocean basin. We propose that the Mn sink associated with the early
762 (and rapid) precipitation of Mn oxide in the water column is characterized by isotopically
763 light Ni relative to seawater, while late-stage Mn sink, occurring over longer time scale and
764 eventually recorded in Fe-Mn crusts, yield Ni isotope composition similar to, or even heavier
765 than seawater. The results of this study also show that formation processes such as
766 precipitation and adsorption processes are the main controls of Ni isotope fractionation and
767 that these processes are dependent on conditions prevailing in the depositional environment.
768 Alternatively, heavier Ni isotopes in Fe-Mn crusts compared to seawater could be explained
769 by the selective incorporation of isotopically heavy Ni species in seawater likely produced by
770 organic complexation (see section 5.1.1.). The Mn sink is the major sink for Ni in the ocean,
771 and we have shown that the Ni isotope composition of the Mn sink is complex. Therefore, a
772 rigorous determination of Ni isotopes in fluxes associated with the Mn sink is required to

balance the oceanic Ni budget, in particular in the authigenic fraction of deep-sea pelagic sediments.

## 6. Summary

In this study, we combined REE and Ni isotope geochemistry in a continuum of samples from pure hydrothermal, hydrothermally-affected by far-field inputs to pure hydrogenetic Fe-Mn deposits from different geological settings and geographical locations. Results show that hydrogenetic Fe-Mn crusts in both the Atlantic and the Pacific oceans have heavy Ni isotope compositions from 0.8 to 1.8 ‰ (with most values comprised between 1.3 and 1.6 ‰), similar to or slightly heavier than seawater value. Rare earth element geochemistry (enriched REE contents, positive Ce anomaly, negative Y anomaly, $Sm_N/Yb_N$ > 0.6) and heavy Ni isotope compositions are the result of Ni removal from seawater through adsorption reactions and structural incorporation of Ni into Mn-oxide minerals.

Hydrothermal deposits from Lo'ihi and Lau Basin have REE-depleted patterns with positive Y anomaly, negative Ce anomaly, and $Sm_N/Yb_N$ < 0.6. However, Ni isotope values are different between the two deposits, Lo'ihi are characterized by $\delta^{60/58}$Ni values between -1.5 ‰ and -0.7 ‰ while LB deposits have heavier $\delta^{60/58}$Ni values from 0.5 ‰ and 1.1 ‰. Extremely light $\delta^{60/58}$Ni values in Lo'ihi are most likely due to the predominance of Fe-oxides which adsorbed isotopically light Ni from seawater or the hydrothermal fluid. By contrast, $\delta^{60/58}$Ni values in LB deposits are interpreted as the result of continuous exchange of Ni with seawater during aging of the deposits.

The Bauer Basin crust and nodules are intermediate because these deposits are characterized by REE-enriched patterns with negative Ce anomaly and flat to negative Y anomaly and isotopically light Ni compared to seawater, i.e., 0.3 ‰ and 0.4 ‰. We suggest

798 that the Ni isotope composition of BB deposits is the result of incorporation of isotopically
799 light Ni from hydrothermal Fe-oxides coming from the East Pacific Rise.
800 We showed that Ni isotopes in the major sink for Ni in the oceans, Fe-Mn oxide
801 phases, are variable and that a proper estimate of each sink flux for each type of deposits
802 would help explaining the imbalance in the Ni oceanic budget. The combination of Ni
803 isotopes with REE geochemistry shows that mineralogy and formation processes is a major
804 control for Ni isotope variability in Fe- and Mn-rich deposits instead of Ni sources.

**Acknowledgements:**

We thank the FeMO team, K. Edwards, C. Moyer, H. Staudigel, B. Tebo, D. Emerson, and B. Glazer and R/V Kilo Moana and ROV Jason II for facilitating access to samples from Hawaii. We thank Harry Elderfield for providing bulk Fe-Mn crusts samples and for thoughtful comments on an earlier version of the manuscript. We thank Marie-Laure Rouget, Yoan Germain and Emmanuel Ponzevera for technical assistance in the clean lab, for ICP-MS and MC-ICP-MS analyses. We thank Sandrine Chéron for XRD analyses. The study was supported by funding from the European Reintegration grant #FP7 #247837, and the LabexMer ANR-10-LABX-19-01.

**Figure captions :**

**Figure 1:** Photographs of the seafloor showing outcrops of (A) Lo'ihi Fe-rich deposits, (B) Apuupuu Fe-Mn crusts (sample J2-480-R11) (C) and Lau Basin Mn-rich deposits (photograph is reproduced from Fouquet et al., 1993), the area showed is ~10 meters large. A section of a bulk Fe-Mn crust sample collected on Apuupuu seamount is shown in (D). Sample locations are shown on the world map (E). Bulk hydrogenetic Pacific and Atlantic Fe-Mn crusts are indicated with red circles, hydrothermal Fe-Mn deposits from Lo'ihi and Lau Basin are displayed in grey, Bauer Basin Fe-Mn deposits are shown in green.

**Figure 2 :** (A) Rare earth elements patterns normalized to PAAS (Post-Archean Australian Shale; Taylor and McLennan, 1995) and (B) Ce/Ce* vs. $Y_N/Ho_N$, in hydrogenetic Fe-Mn crusts (red), Bauer Basin Fe-Mn deposits (green), and Lo'ihi (grey) and Lau Basin hydrothermal deposits (pink).

**Figure 3 :** Plot of (A) Co/Mn, (B) Cu/Mn and (C) Zn/Mn versus Ni/Mn ratios in bulk hydrogenetic Fe-Mn crusts (red) and Bauer Basin Fe-Mn deposits (green), and hydrothermal Fe-Mn deposits from Lo'ihi (grey) and Lau Basin (pink).

**Figure 4**: Nickel isotope composition (‰) versus (A) Ni/Mn and (B) Fe/Mn ratios in hydrogenetic Fe-Mn crusts (red), Bauer Basin Fe-Mn deposits (green), Lo'ihi hydrothermal deposits (grey) and Lau Basin hydrothermal deposits (pink).

**Figure 5 :** (A) Nickel isotope composition versus depth of deposition of hydrogenetic Fe-Mn crusts, and (B) distribution of Ni isotope values of hydrogenetic Fe-Mn crusts. The values

represented include data from Gall et al. (2013), Gueguen et al. (2016) and data from this study.

**Figure 6 :** Nickel isotope composition versus (A) Ce/Ce*, (B) $Y_N/Ho_N$ and (C) $Sm_N/Yb_N$ in hydrogenetic Fe-Mn crusts (red), Bauer Basin Fe-Mn crust (green), Lo'ihi hydrothermal deposits (grey) and Lau Basin hydrothermal deposits (pink). The Ce anomaly is defined as $Ce/Ce^* = Ce_N/(Pr_N^2/Nd_N)$ (Lawrence et al., 2006). This figure allows distinguishing between three groups of samples: (1) hydrogenetic Fe-Mn crusts with positive Ce anomalies and $\delta^{60/58}Ni$ values falling in the range of seawater, (2) hydrothermal deposits from Lo'ihi with no Ce anomalies and light $\delta^{60/58}Ni$ values, and (3) Bauer Basin and Lau Basin Fe-Mn deposits displaying negative Ce anomalies and $\delta^{60/58}Ni$ values that are lighter than seawater values.

**Table captions:**

**Table 1**: Nickel isotope composition (‰), selected elemental ratios (µg/µg), and Ce/Ce* (Ce anomaly) and $Y_N/Ho_N$ (Y anomaly) of Fe-Mn deposits.

**Supplementary material:**

**Table S1:** Sampling information and mineralogy (X-Ray diffraction) of bulk hydrogenetic Fe-Mn crusts and nodules, and Lau Basin Fe-Mn deposits.

**Table S2:** Geochemical composition (µg/g) of Fe-Mn deposits.

**References:**


Aplin, A.C., Cronan, D.S., 1985. Ferromanganese oxide deposits from the Central Pacific ocean. 1. Encrustations from the Line islands archipelago. Geochimica Et Cosmochimica Acta, 49(2): 427-436.

Archer, C., Vance, D., Milne, A., Lohan, M.C., 2020. The oceanic biogeochemistry of nickel and its isotopes: New data from the South Atlantic and the Southern Ocean biogeochemical divide. Earth and Planetary Science Letters, 535: 116118.

Bau, M., 1999. Scavenging of dissolved yttrium and rare earths by precipitating iron oxyhydroxide: experimental evidence for Ce oxidation, Y-Ho fractionation, and lanthanide tetrad effect. Geochimica Et Cosmochimica Acta, 63(1): 67-77.

Bau, M., Koschinsky, A., 2009. Oxidative scavenging of cerium on hydrous Fe oxide: Evidence from the distribution of rare earth elements and yttrium between Fe oxides and Mn oxides in hydrogenetic ferromanganese crusts. Geochemical Journal, 43(1): 37-47.

Bau, M., Koschinsky, A., Dulski, P., Hein, J.R., 1996. Comparison of the partitioning behaviours of yttrium, rare earth elements, and titanium between hydrogenetic marine ferromanganese crusts and seawater. Geochimica Et Cosmochimica Acta, 60(10): 1709-1725.

Bau, M., Schmidt, K., Koschinsky, A., Hein, J., Kuhn, T., Usui, A., 2014. Discriminating between different genetic types of marine ferro-manganese crusts and nodules based on rare earth elements and yttrium. Chemical Geology, 381(0): 1-9.

Bonatti, E., Kraemer, T., Rydell, H., 1972. Classification and genesis of submarine iron-manganese deposits, Ferromanganese deposits on the Ocean Floor. Washington DC, Nat. Sci. Found., pp. 149-165.

Boström, K., Peterson, M.N.A., Joensuu, O., Fisher, D.E., 1969. Aluminum-poor ferromanganoan sediments on active oceanic ridges. Journal of Geophysical Research, 74(12): 3261-3270.

Bruland, K.W., 1980. Oceanographic distributions of Cadmium, Zinc, Nickel, and Copper in the North Pacific. Earth and Planetary Science Letters, 47(2): 176-198.

Cameron, V., Vance, D., 2014. Heavy nickel isotope compositions in rivers and the oceans. Geochimica Et Cosmochimica Acta, 128(0): 195-211.

Chu, N.C., Johnson, C.M., Beard, B.L., German, C.R., Nesbitt, R.W., Frank, M., Bohn, M., Kubik, P.W., Usui, A., Graham, I., 2006. Evidence for hydrothermal venting in Fe isotope compositions of the deep Pacific Ocean through time. Earth and Planetary Science Letters, 245(1-2): 202-217.

Ciscato, E.R., Bontognali, T.R.R., Vance, D., 2018. Nickel and its isotopes in organic-rich sediments: implications for oceanic budgets and a potential record of ancient seawater. Earth and Planetary Science Letters, 494: 239-250.

Conway, T.M., John, S.G., 2014. Quantification of dissolved iron sources to the North Atlantic Ocean. Nature, 511(7508): 212-215.

De Baar, H.J.W., Bacon, M.P., Brewer, P.G., Bruland, K.W., 1985. Rare Earth elements in the Pacific and Atlantic Oceans. Geochimica Et Cosmochimica Acta, 49(9): 1943-1959.

De Carlo, E.H., McMurtry, G.M., Kim, K.H., 1987. Geochemistry of ferromanganese crusts from the hawaiian archipelago. 1. Northern survey areas. Deep-Sea Research Part a-Oceanographic Research Papers, 34(3): 441-467.

Douville, E., Charlou, J.L., Oelkers, E.H., Bienvenu, P., Colon, C.F.J., Donval, J.P., Fouquet, Y., Prieur, D., Appriou, P., 2002. The rainbow vent fluids (36 degrees 14 ' N, MAR): the influence of ultramafic rocks and phase separation on trace metal content in Mid-Atlantic Ridge hydrothermal fluids. Chemical Geology, 184(1-2): 37-48.

Dymond, J., Veeh, H.H., 1975. Metal accumulation rates in the Southeast Pacific and the origin of metalliferous sediments. Earth and Planetary Science Letters, 28(1): 13-22.

Edwards, K.J., Glazer, B.T., Rouxel, O.J., Bach, W., Emerson, D., Davis, R.E., Toner, B.M., Chan, C.S., Tebo, B.M., Staudigel, H., Moyer, C.L., 2011. Ultra-diffuse hydrothermal venting supports Fe-oxidizing bacteria and massive umber deposition at 5000m off Hawaii. The ISME journal: 1-11.

Elderfield, H., Greaves, M.J., 1981. Negative Cerium anomalies in the rare-earth element patterns of oceanic ferromanganese nodules. Earth and Planetary Science Letters, 55(1): 163-170.

Elderfield, H., Hawkesworth, C.J., Greaves, M.J., Calvert, S.E., 1981a. Rare-earth element geochemistry of oceanic ferromanganese nodules and associated sediments. Geochimica Et Cosmochimica Acta, 45(4): 513-528.

Elderfield, H., Hawkesworth, C.J., Greaves, M.J., Calvert, S.E., 1981b. Rare-earth element zonation in Pacific ferromanganese nodules. Geochimica Et Cosmochimica Acta, 45(7): 1231-1234.

Elderfield, H., Schultz, A., 1996. Mid-ocean ridge hydrothermal fluxes and the chemical composition of the ocean. Annual Review of Earth and Planetary Sciences, 24: 191-224.

Elderfield, H., Whitfield, M., Burton, J.D., Bacon, M.P., Liss, P.S., 1988. The Oceanic Chemistry of the Rare-Earth Elements. Philosophical Transactions of the Royal Society of London. Series A, Mathematical and Physical Sciences, 325(1583): 105-126.

Emerson, D., Moyer, C.L., 2002. Neutrophilic Fe-Oxidizing Bacteria Are Abundant at the Loihi Seamount Hydrothermal Vents and Play a Major Role in Fe Oxide Deposition. Applied and Environmental Microbiology, 68(6): 3085-3093.

Fitzsimmons, J.N., Boyle, E.A., Jenkins, W.J., 2014. Distal transport of dissolved hydrothermal iron in the deep South Pacific Ocean. Proceedings of the National Academy of Sciences, 111(47): 16654-16661.

Fouquet, Y., von Stackelberg, U., Charlou, J.L., Donval, J.P., Foucher, J.P., Erzinger, J., Herzig, P., Mühe, R., Wiedicke, M., Soakai, S., Whitechurch, H., 1991. Hydrothermal activity in the Lau back-arc basin:Sulfides and water chemistry. Geology, 19(4): 303-306.

940 Fouquet, Y., von Stackelberg, U., Charlou, J.L., Erzinger, J., Herzig, P.M., Muehe, R.,
941 Wiedicke, M., 1993. Metallogenesis in back-arc environments: the Lau Basin example.
942 Economic Geology, 88(8): 2154-2181.

943 Frank, M., 2002. Radiogenic isotopes: Tracers of past ocean circulation and erosional input.
944 Reviews of Geophysics, 40(1).

945 Frank, M., O'Nions, R.K., Hein, J.R., Banakar, V.K., 1999. 60 Myr records of major elements
946 and Pb–Nd isotopes from hydrogenous ferromanganese crusts: reconstruction of seawater
947 paleochemistry. Geochimica Et Cosmochimica Acta, 63(11–12): 1689-1708.

948 Frank, M., Whiteley, N., Kasten, S., Hein, J.R., O'Nions, K., 2002. North Atlantic deep water
949 export to the Southern Ocean over the past 14 Myr: Evidence from Nd and Pb isotopes in
950 ferromanganese crusts. Paleoceanography, 17(2).

951 Fujii, T., Moynier, F., Dauphas, N., Abe, M., 2011. Theoretical and experimental
952 investigation of nickel isotopic fractionation in species relevant to modern and ancient oceans.
953 Geochimica et Cosmochimica Acta, 75(2): 469-482.

954 Gall, L., Williams, H.M., Siebert, C., Halliday, A.N., Herrington, R.J., Hein, J.R., 2013.
955 Nickel isotopic compositions of ferromanganese crusts and the constancy of deep ocean
956 inputs and continental weathering effects over the Cenozoic. Earth and Planetary Science
957 Letters, 375(0): 148-155.

958 German, C.R., Klinkhammer, G.P., Edmond, J.M., Mitra, A., Elderfield, H., 1990.
959 Hydrothermal scavenging of rare earth elements in the ocean. Nature, 345(6275): 516-518.

960 German, C.R., Seyfried, W.E., 2014. Hydrothermal Processes. In: Turekian, K.K., Holland,
961 H.D. (Eds.), Treatise on Geochemistry (Second Edition). Elsevier, Oxford, pp. 191-233.

962 Glazer, B.T., Rouxel, O.J., 2009. Redox Speciation and Distribution within Diverse Iron-
963 dominated Microbial Habitats at Loihi Seamount. Geomicrobiology Journal, 26(8): 606 - 622.

964 Gueguen, B., Rouxel, O., Ponzevera, E., Bekker, A., Fouquet, Y., 2013. Nickel Isotope
965 Variations in Terrestrial Silicate Rocks and Geological Reference Materials Measured by
966 MC-ICP-MS. Geostandards and Geoanalytical Research, 37(3): 297-317.

967 Gueguen, B., Rouxel, O., Rouget, M.-L., Bollinger, C., Ponzevera, E., Germain, Y., Fouquet,
968 Y., 2016. Comparative geochemistry of four ferromanganese crusts from the Pacific Ocean
969 and significance for the use of Ni isotopes as paleoceanographic tracers. Geochimica et
970 Cosmochimica Acta, 189: 214-235.

971 Gueguen, B., Sorensen, J.V., Lalonde, S.V., Peña, J., Toner, B.M., Rouxel, O., 2018. Variable
972 Ni isotope fractionation between Fe-oxyhydroxides and implications for the use of Ni
973 isotopes as geochemical tracers. Chemical Geology, 481: 38-52.

974 Halbach, P., Puteanus, D., 1984. The influence of the carbonate dissolution rate on the growth
975 and composition of Co-rich ferromanganese crusts from Central Pacific seamount areas. Earth
976 and Planetary Science Letters, 68(1): 73-87.

977 Halbach, P., Puteanus, D., Manheim, F.T., 1984. Platinum concentrations in ferromanganese
978 seamount crusts from the Central Pacific. Naturwissenschaften, 71(11): 577-579.

979 Hannington, M.D., 2013. The role of black smokers in the Cu mass balance of the oceanic
980 crust. Earth and Planetary Science Letters(0).

981 Heath, G.R., Dymond, J., 1977. Genesis and transformation of metalliferous sediments from
982 East Pacific rise, Bauer deep, and Central basin, Northwest Nazca plate. Geological Society of
983 America Bulletin, 88(5): 723-733.

984 Hein, J.R., Koschinsky, A., 2014. Deep-Ocean Ferromanganese Crusts and Nodules. In:
985 Holland, H.D., Turekian, K.K. (Eds.), Treatise on Geochemistry (Second Edition). Elsevier,
986 Oxford, pp. 273-291.

987 Hein, J.R., Koschinsky, A., Halliday, A.N., 2003. Global occurrence of tellurium-rich
988 ferromanganese crusts and a model for the enrichment of tellurium. Geochimica et
989 Cosmochimica Acta, 67(6): 1117-1127.

990 Hein, J.R., Mizell, K., Koschinsky, A., Conrad, T.A., 2013. Deep-ocean mineral deposits as a
991 source of critical metals for high- and green-technology applications: Comparison with land-
992 based resources. Ore Geology Reviews, 51(0): 1-14.

993 Hem, J.D., 1978. Redox processes at surfaces of manganese oxide and their effects on
994 aqueous metal ions. Chemical Geology, 21(3–4): 199-218.

995 Horner, T.J., Williams, H.M., Hein, J.R., Saito, M.A., Burton, K.W., Halliday, A.N., Nielsen,
996 S.G., 2015. Persistence of deeply sourced iron in the Pacific Ocean. Proceedings of the
997 National Academy of Sciences.

998 John, S.G., Rouxel, O.J., Craddock, P.R., Engwall, A.M., Boyle, E.A., 2008. Zinc stable
999 isotopes in seafloor hydrothermal vent fluids and chinmeys. Earth and Planetary Science
1000 Letters, 269(1-2): 17-28.

1001 Klaver, M., Ionov, D.A., Takazawa, E., Elliott, T., 2020. The non-chondritic Ni isotope
1002 composition of Earth's mantle. Geochimica et Cosmochimica Acta, 268: 405-421.

1003 Klemm, V., Levasseur, S., Frank, M., Hein, J.R., Halliday, A.N., 2005. Osmium isotope
1004 stratigraphy of a marine ferromanganese crust. Earth and Planetary Science Letters, 238(1-2):
1005 42-48.

1006 Klemm, V., Reynolds, B., Frank, M., Pettke, T., Halliday, A.N., 2007. Cenozoic changes in
1007 atmospheric lead recorded in central Pacific ferromanganese crusts. Earth and Planetary
1008 Science Letters, 253(1-2): 57-66.

1009 Klinkhammer, G., Hudson, A., 1986. Dispersal patterns for hydrothermal plumes in the South
1010 Pacific using manganese as a tracer. Earth and Planetary Science Letters, 79(3): 241-249.

1011 Klinkhammer, G.P., Bender, M.L., 1980. The distribution of manganese in the Pacific Ocean.
1012 Earth and Planetary Science Letters, 46(3): 361-384.

1013 Koschinsky, A., Halbach, P., 1995. Sequential leaching of marine ferromanganese
1014 precipitates: Genetic implications. Geochimica et Cosmochimica Acta, 59(24): 5113-5132.

1015 Koschinsky, A., Hein, J.R., 2003. Uptake of elements from seawater by ferromanganese
1016 crusts: solid-phase associations and seawater speciation. Marine Geology, 198(3-4): 331-351.

1017 Koschinsky, A., Winkler, A., Fritsche, U., 2003. Importance of different types of marine
1018 particles for the scavenging of heavy metals in the deep-sea bottom water. Applied
1019 Geochemistry, 18(5): 693-710.

1020 Kuhn, T., Bau, M., Blum, N., Halbach, P., 1998. Origin of negative Ce anomalies in mixed
1021 hydrothermal–hydrogenetic Fe–Mn crusts from the Central Indian Ridge. Earth and Planetary
1022 Science Letters, 163(1–4): 207-220.

1023 Lam, P.J., Lee, J.-M., Heller, M.I., Mehic, S., Xiang, Y., Bates, N.R., 2018. Size-fractionated
1024 distributions of suspended particle concentration and major phase composition from the U.S.
1025 GEOTRACES Eastern Pacific Zonal Transect (GP16). Marine Chemistry, 201: 90-107.

1026 Lawrence, M.G., Greig, A., Collerson, K.D., Kamber, B.S., 2006. Rare Earth Element and
1027 Yttrium Variability in South East Queensland Waterways. Aquatic Geochemistry, 12(1): 39-
1028 72.

1029 Lee, J.-M., Heller, M.I., Lam, P.J., 2018. Size distribution of particulate trace elements in the
1030 U.S. GEOTRACES Eastern Pacific Zonal Transect (GP16). Marine Chemistry, 201: 108-123.

1031 Little, S.H., Archer, C., McManus, J., Najorka, J., Wegorzewski, A.V., Vance, D., 2020.
1032 Towards balancing the oceanic Ni budget. Earth and Planetary Science Letters, 547: 116461.

1033 Little, S.H., Vance, D., Walker-Brown, C., Landing, W.M., 2014. The oceanic mass balance
1034 of copper and zinc isotopes, investigated by analysis of their inputs, and outputs to
1035 ferromanganese oxide sediments. Geochimica et Cosmochimica Acta, 125(0): 673-693.

1036 Lyle, M., Dymond, J., Ross Heath, G., 1977. Copper-nickel-enriched ferromanganese nodules
1037 and associated crusts from the Bauer Basin, northwest Nazca plate. Earth and Planetary
1038 Science Letters, 35(1): 55-64.

1039 Mills, R.A., Wells, D.M., Roberts, S., 2001. Genesis of ferromanganese crusts from the TAG
1040 hydrothermal field. Chemical Geology, 176(1–4): 283-293.

1041 Mizell, K., Hein, J.R., Lam, P.J., Koppers, A.A.P., Staudigel, H., 2020. Geographic and
1042 Oceanographic Influences on Ferromanganese Crust Composition Along a Pacific Ocean
1043 Meridional Transect, 14 N to 14S. Geochemistry, Geophysics, Geosystems, 21(2):
1044 e2019GC008716.

1045 Moffett, J.W., 1990. Microbially mediated cerium oxidation in sea water. Nature, 345(6274):
1046 421-423.

1047 Moffett, J.W., 1994. The relationship between cerium and manganese oxidation in the marine
1048 environment. Limnology and Oceanography, 39(6): 1309-1318.

1049 Mohwinkel, D., Kleint, C., Koschinsky, A., 2014. Phase associations and potential selective
1050 extraction methods for selected high-tech metals from ferromanganese nodules and crusts
1051 with siderophores. Applied Geochemistry, 43: 13-21.

1052 Morel, F.M.M., Milligan, A.J., Saito, M.A., 2014. Marine Bioinorganic Chemistry: The Role
1053 of Trace Metals in the Oceanic Cycles of Major Nutrients. In: Turekian, K.K. (Ed.), Treatise
1054 on Geochemistry (Second Edition). Elsevier, Oxford, pp. 123-150.

Mottl, M.J., Seewald, J.S., Wheat, C.G., Tivey, M.K., Michael, P.J., Proskurowski, G., McCollom, T.M., Reeves, E., Sharkey, J., You, C.F., Chan, L.H., Pichler, T., 2011. Chemistry of hot springs along the Eastern Lau Spreading Center. Geochimica et Cosmochimica Acta, 75(4): 1013-1038.

Nielsen, S.G., Gannoun, A., Marnham, C., Burton, K.W., Halliday, A.N., Hein, J.R., 2011. New age for ferromanganese crust 109D-C and implications for isotopic records of lead, neodymium, hafnium, and thallium in the Pliocene Indian Ocean. Paleoceanography, 26.

O'Nions, R.K., Frank, M., von Blanckenburg, F., Ling, H.F., 1998. Secular variation of Nd and Pb isotopes in ferromanganese crusts from the Atlantic, Indian and Pacific Oceans. Earth and Planetary Science Letters, 155(1-2): 15-28.

Peacock, C.L., 2009. Physiochemical controls on the crystal-chemistry of Ni in birnessite: Genetic implications for ferromanganese precipitates. Geochimica et Cosmochimica Acta, 73(12): 3568-3578.

Peacock, C.L., Sherman, D.M., 2007a. Sorption of Ni by birnessite: Equilibrium controls on Ni in seawater. Chemical Geology, 238(1-2): 94-106.

Peacock, C.L., Sherman, D.M., 2007b. Crystal-chemistry of Ni in marine ferromanganese crusts and nodules. American Mineralogist, 92(7): 1087-1092.

Price, N.M., Morel, F.M.M., 1991. Colimitation of phytoplankton growth by Nickel and Nitrogen. Limnology and Oceanography, 36(6): 1071-1077.

Ravizza, G., McMurtry, G.M., 1993. Osmium isotopic variations in metalliferous sediments from the East Pacific Rise and the Bauer Basin. Geochimica Et Cosmochimica Acta, 57(17): 4301-4310.

Resing, J.A., Sedwick, P.N., German, C.R., Jenkins, W.J., Moffett, J.W., Sohst, B.M., Tagliabue, A., 2015. Basin-scale transport of hydrothermal dissolved metals across the South Pacific Ocean. Nature, 523(7559): 200-203.

Reynolds, B.C., Frank, M., O'Nions, R.K., 1999. Nd- and Pb-isotope time series from Atlantic ferromanganese crusts: implications for changes in provenance and paleocirculation over the last 8 Myr. Earth and Planetary Science Letters, 173(4): 381-396.

Rouxel, O., Toner, B., Germain, Y., Glazer, B., 2018. Geochemical and iron isotopic insights into hydrothermal iron oxyhydroxide deposit formation at Loihi Seamount. Geochimica et Cosmochimica Acta, 220: 449-482.

Rouxel, O., Toner, B.M., Manganini, S.J., German, C.R., 2016. Geochemistry and iron isotope systematics of hydrothermal plume fall-out at East Pacific Rise 9°50′N. Chemical Geology, 441: 212-234.

Saito, M.A., Noble, A.E., Tagliabue, A., Goepfert, T.J., Lamborg, C.H., Jenkins, W.J., 2013. Slow-spreading submarine ridges in the South Atlantic as a significant oceanic iron source. Nature Geosci, advance online publication.

1092 Saito, M.A., Sigman, D.M., Morel, F.M.M., 2003. The bioinorganic chemistry of the ancient
1093 ocean: the co-evolution of cyanobacterial metal requirements and biogeochemical cycles at
1094 the Archean-Proterozoic boundary? Inorganica Chimica Acta, 356: 308-318.

1095 Sclater, F.R., Boyle, E., Edmond, J.M., 1976. On the marine geochemistry of nickel. Earth
1096 and Planetary Science Letters, 31(1): 119-128.

1097 Sedwick, P.N., McMurtry, G.M., Macdougall, J.D., 1992. Chemistry of hydrothermal
1098 solutions from Pele vents, Loihi seamount, Hawaii. Geochimica Et Cosmochimica Acta,
1099 56(10): 3643-3667.

1100 Siebert, C., Nagler, T.F., Kramers, J.D., 2001. Determination of molybdenum isotope
1101 fractionation by double-spike multicollector inductively coupled plasma mass spectrometry.
1102 Geochemistry Geophysics Geosystems, 2: 1032.

1103 Sorensen, J.V., Gueguen, B., Stewart, B.D., Peña, J., Rouxel, O., Toner, B.M., 2020. Large
1104 nickel isotope fractionation caused by surface complexation reactions with hexagonal
1105 birnessite. Chemical Geology, 537: 119481.

1106 Tagliabue, A., Aumont, O., Bopp, L., 2014. The impact of different external sources of iron
1107 on the global carbon cycle. Geophysical Research Letters: 2013GL059059.

1108 Tagliabue, A., Bopp, L., Dutay, J.C., Bowie, A.R., Chever, F., Jean-Baptiste, P., Bucciarelli,
1109 E., Lannuzel, D., Remenyi, T., Sarthou, G., Aumont, O., Gehlen, M., Jeandel, C., 2010.
1110 Hydrothermal contribution to the oceanic dissolved iron inventory. Nature Geoscience, 3(4):
1111 252-256.

1112 Takano, S., Tanimizu, M., Hirata, T., Shin, K.-C., Fukami, Y., Suzuki, K., Sohrin, Y., 2017.
1113 A simple and rapid method for isotopic analysis of nickel, copper, and zinc in seawater using
1114 chelating extraction and anion exchange. Analytica Chimica Acta, 967: 1-11.

1115 Taylor, S.R., McLennan, S.M., 1995. The geochemical evolution of the continental crust.
1116 Reviews of Geophysics, 33(2): 241-265.

1117 Toner, B.M., Berquó, T.S., Michel, F.M., Sorensen, J.V., Templeton, A.S., Edwards, K.J.,
1118 2012. Mineralogy of iron microbial mats from loihi seamount. Frontiers in microbiology, 3.

1119 Toner, B.M., Fakra, S.C., Manganini, S.J., Santelli, C.M., Marcus, M.A., Moffett, J., Rouxel,
1120 O., German, C.R., Edwards, K.J., 2009. Preservation of iron(II) by carbon-rich matrices in a
1121 hydrothermal plume. Nature Geoscience, 2(3): 197-201.

1122 van de Flierdt, T., Frank, M., Halliday, A.N., Hein, J.R., Hattendorf, B., Günther, D., Kubik,
1123 P.W., 2004. Tracing the history of submarine hydrothermal inputs and the significance of
1124 hydrothermal hafnium for the seawater budget—a combined Pb–Hf–Nd isotope approach.
1125 Earth and Planetary Science Letters, 222(1): 259-273.

1126 Vance, D., Little, S.H., Archer, C., Cameron, V., Andersen, M.B., Rijkenberg, M.J.A., Lyons,
1127 T.W., 2016. The oceanic budgets of nickel and zinc isotopes: the importance of sulfidic
1128 environments as illustrated by the Black Sea. Philosophical Transactions of the Royal Society
1129 A: Mathematical, Physical and Engineering Sciences, 374(2081).

Von Damm, K.L., 1995. Controls on the Chemistry and Temporal Variability of Seafloor Hydrothermal Fluids, Seafloor Hydrothermal Systems: Physical, Chemical, Biological, and Geological Interactions. American Geophysical Union, Geophysical Monograph Series, pp. 222-247.

Wang, R.M., Archer, C., Bowie, A.R., Vance, D., 2019. Zinc and nickel isotopes in seawater from the Indian Sector of the Southern Ocean: The impact of natural iron fertilization versus Southern Ocean hydrography and biogeochemistry. Chemical Geology, 511: 452-464.

Wasylenki, L.E., Howe, H.D., Spivak-Birndorf, L.J., Bish, D.L., 2015. Ni isotope fractionation during sorption to ferrihydrite: Implications for Ni in banded iron formations. Chemical Geology, 400(0): 56-64.

Wasylenki, L.E., Swihart, J.W., Romaniello, S.J., 2014. Cadmium isotope fractionation during adsorption to Mn oxyhydroxide at low and high ionic strength. Geochimica et Cosmochimica Acta, 140(0): 212-226.

Wegorzewski, A.V., Grangeon, S., Webb, S.M., Heller, C., Kuhn, T., 2020. Mineralogical transformations in polymetallic nodules and the change of Ni, Cu and Co crystal-chemistry upon burial in sediments. Geochimica et Cosmochimica Acta, 282: 19-37.

Wheat, C.G., Jannasch, H.W., Kastner, M., Plant, J.N., DeCarlo, E.H., 2003. Seawater transport and reaction in upper oceanic basaltic basement: chemical data from continuous monitoring of sealed boreholes in a ridge flank environment. Earth and Planetary Science Letters, 216(4): 549-564.

Wheat, C.G., Jannasch, H.W., Plant, J.N., Moyer, C.L., Sansone, F.J., McMurtry, G.M., 2000. Continuous sampling of hydrothermal fluids from Loihi Seamount after the 1996 event. Journal of Geophysical Research-Solid Earth, 105(B8): 19353-19367.

Wheat, C.G., Mottl, M.J., Rudnicki, M., 2002. Trace element and REE composition of a low-temperature ridge-flank hydrothermal spring. Geochimica Et Cosmochimica Acta, 66(21): 3693-3705.

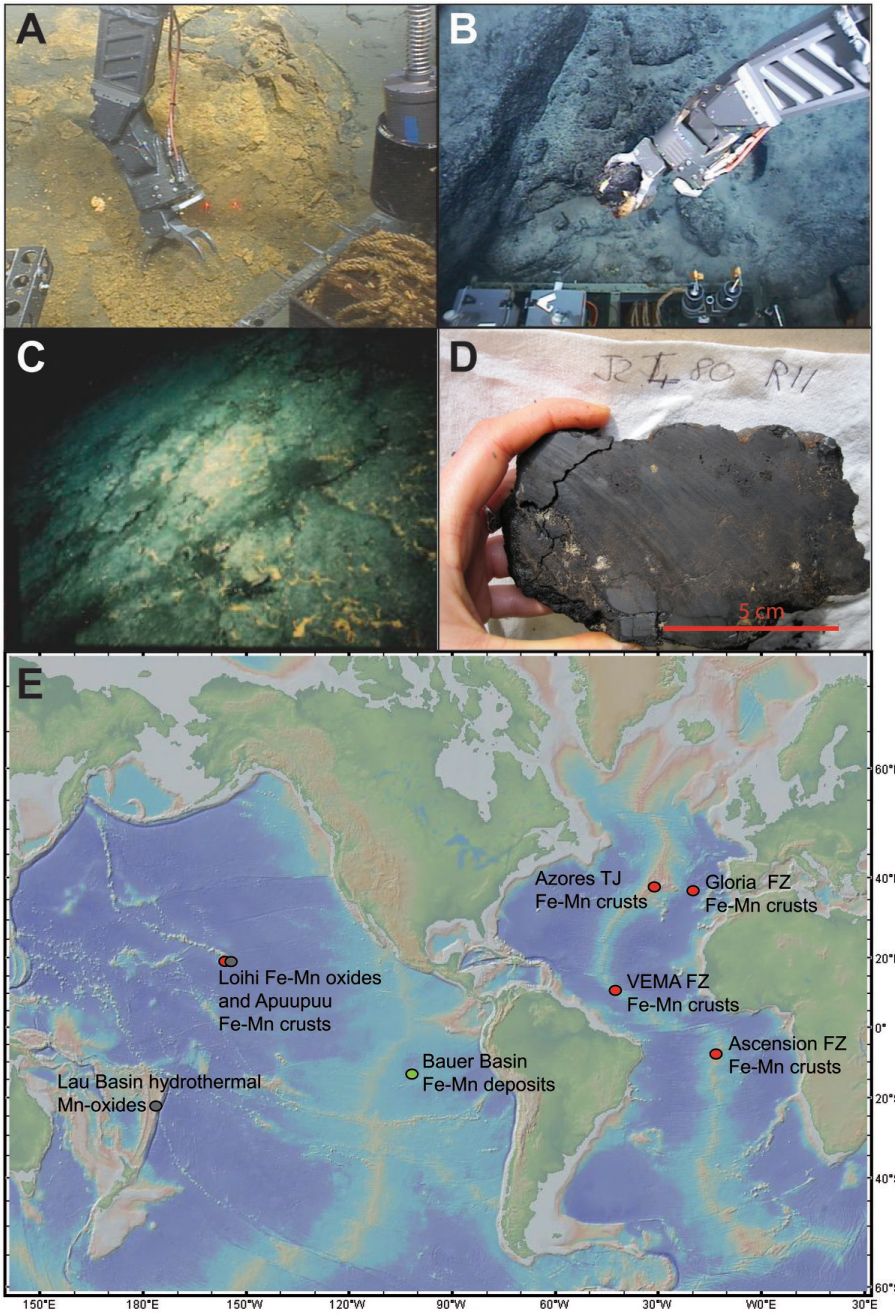
A
B
C
D
JR 4 80 R11
5 cm
E
Azores TJ
Fe-Mn crusts
Gloria FZ
Fe-Mn crusts
Loihi Fe-Mn oxides
and Apuupuu
Fe-Mn crusts
VEMA FZ
Fe-Mn crusts
Ascension FZ
Fe-Mn crusts
Bauer Basin
Fe-Mn deposits
Lau Basin hydrothermal
Mn-oxides
60°N
40°N
20°N
0°
20°S
40°S
60°S
150°E
180°E
150°W
120°W
90°W
60°W
30°W
W0°E
30°E

Figure 1

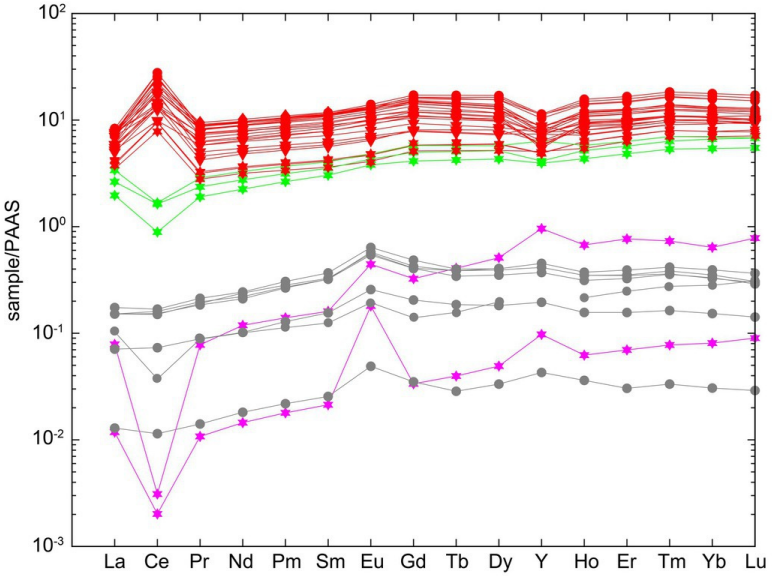
sample/PAAS
$10^2$
$10^1$
$10^0$
$10^{-1}$
$10^{-2}$
$10^{-3}$
La Ce Pr Nd Pm Sm Eu Gd Tb Dy Y Ho Er Tm Yb Lu

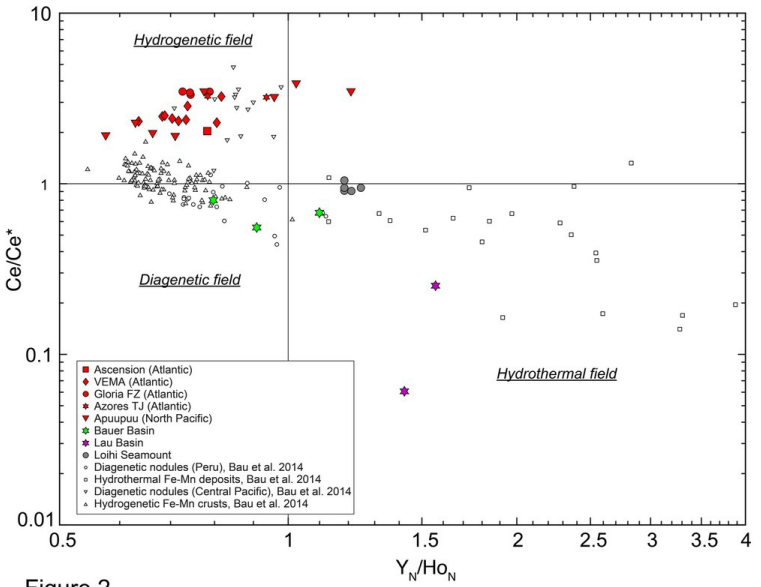
Hydrogenetic field
Diagenetic field
Hydrothermal field
Ce/Ce*
$Y_N/Ho_N$
10
1
0.1
0.01
0.5
1
1.5
2
2.5
3
3.5
4
Ascension (Atlantic)
VEMA (Atlantic)
Gloria FZ (Atlantic)
Azores TJ (Atlantic)
Apuupuu (North Pacific)
Bauer Basin
Lau Basin
Loihi Seamount
Diagenetic nodules (Peru), Bau et al. 2014
Hydrothermal Fe-Mn deposits, Bau et al. 2014
Diagenetic nodules (Central Pacific), Bau et al. 2014
Hydrogenetic Fe-Mn crusts, Bau et al. 2014

Figure 2

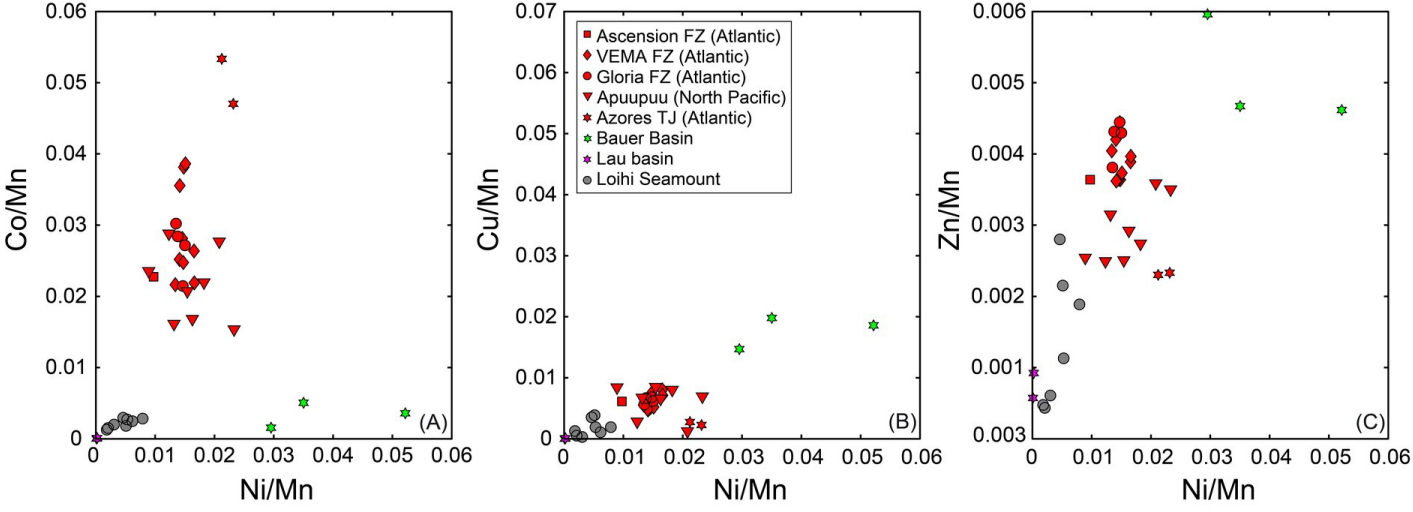
Co/Mn
Ni/Mn
(A)
Cu/Mn
Ni/Mn
(B)
Zn/Mn
Ni/Mn
(C)
Ascension FZ (Atlantic)
VEMA FZ (Atlantic)
Gloria FZ (Atlantic)
Apuupuu (North Pacific)
Azores TJ (Atlantic)
Bauer Basin
Lau basin
Loihi Seamount

Figure 3

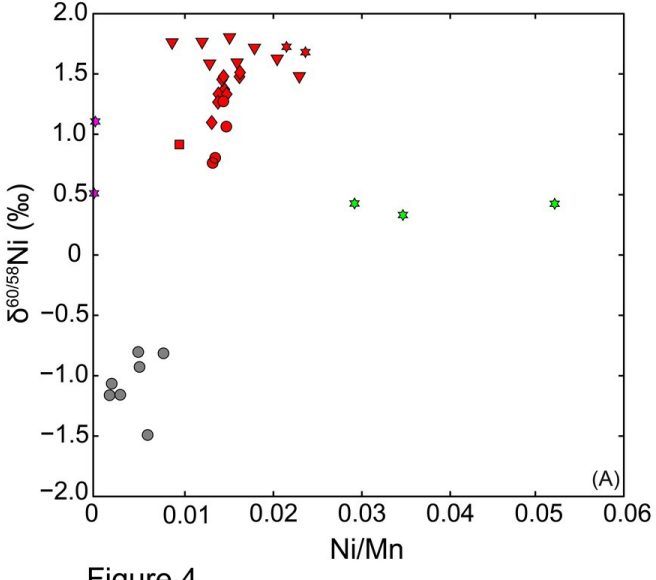
2.0
1.5
1.0
0.5
0
−0.5
−1.0
−1.5
−2.0
δ60/58Ni (‰)
0
0.01
0.02
0.03
0.04
0.05
0.06
Ni/Mn
(A)

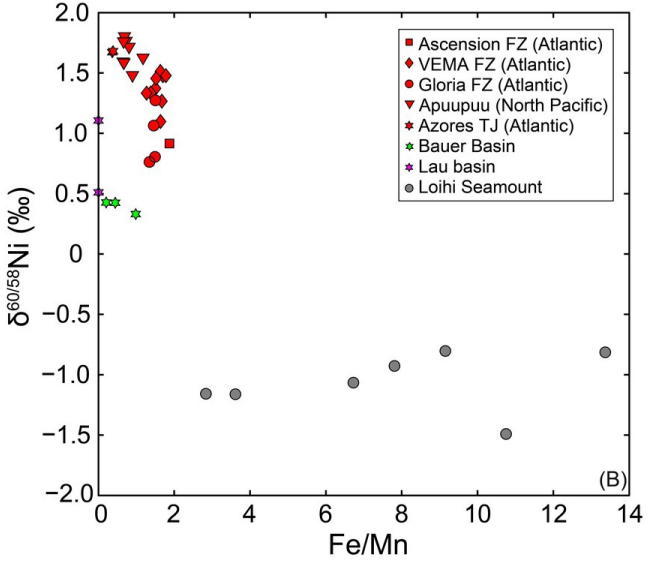
Ascension FZ (Atlantic)
VEMA FZ (Atlantic)
Gloria FZ (Atlantic)
Apuupuu (North Pacific)
Azores TJ (Atlantic)
Bauer Basin
Lau basin
Loihi Seamount
2.0
1.5
1.0
0.5
0
−0.5
−1.0
−1.5
−2.0
δ60/58Ni (‰)
0
2
4
6
8
10
12
14
Fe/Mn
(B)

Figure 4

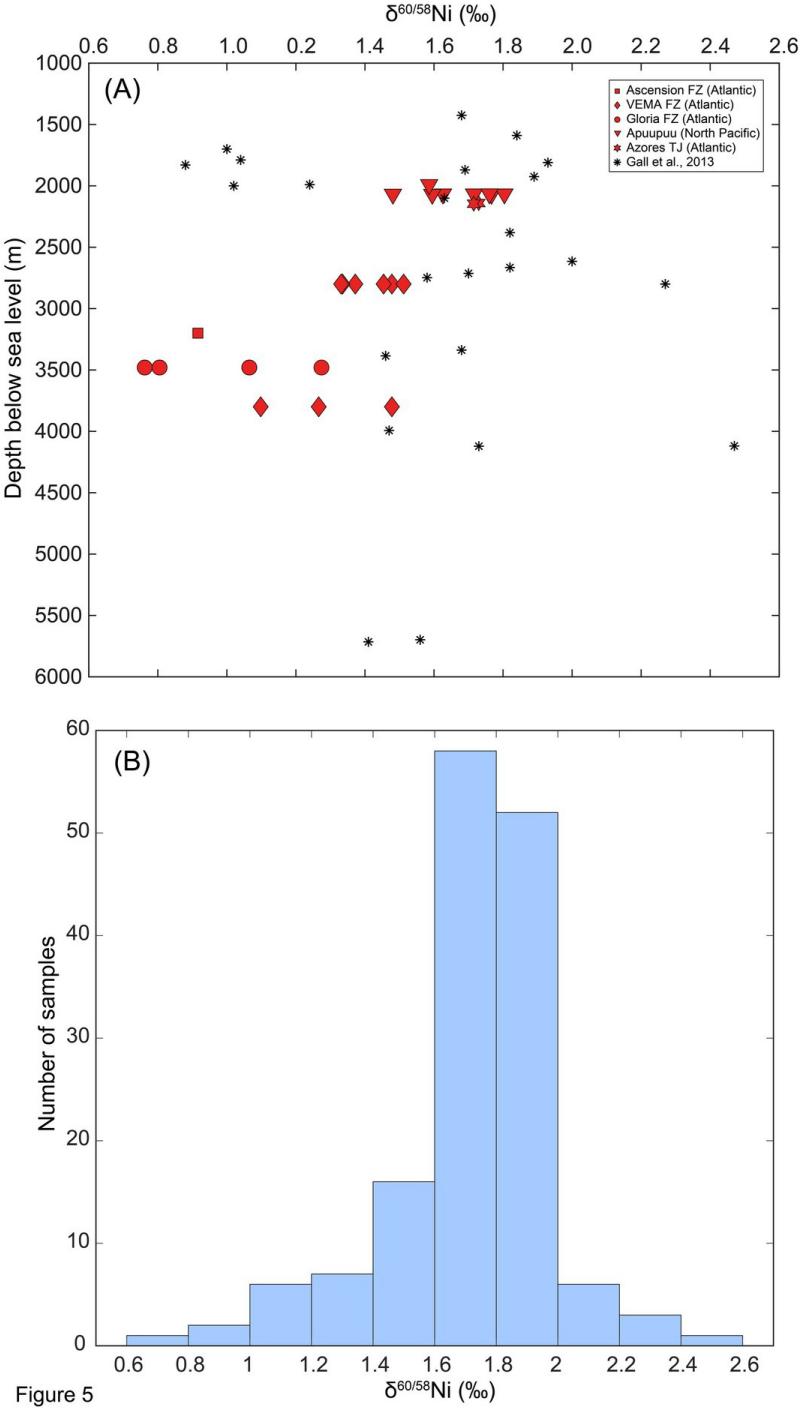
(A)
δ60/58Ni (‰)
0.6
0.8
1.0
0.2
1.4
1.6
1.8
2.0
2.2
2.4
2.6
Depth below sea level (m)
1000
1500
2000
2500
3000
3500
4000
4500
5000
5500
6000
Ascension FZ (Atlantic)
VEMA FZ (Atlantic)
Gloria FZ (Atlantic)
Apuupuu (North Pacific)
Azores TJ (Atlantic)
Gall et al., 2013
(B)
Number of samples
60
50
40
30
20
10
0
0.6
0.8
1
1.2
1.4
1.6
1.8
2
2.2
2.4
2.6
δ60/58Ni (‰)

Figure 5

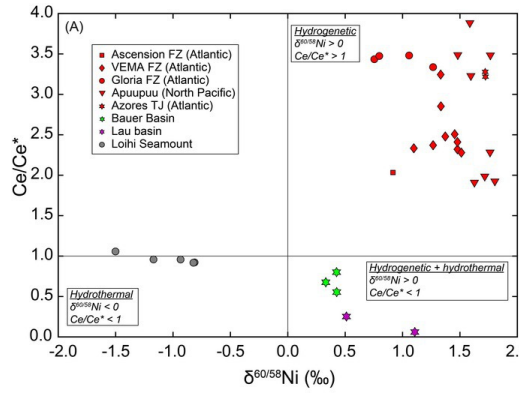
(A)
Ce/Ce*
δ60/58Ni (‰)
Ascension FZ (Atlantic)
VEMA FZ (Atlantic)
Gloria FZ (Atlantic)
Apuupuu (North Pacific)
Azores TJ (Atlantic)
Bauer Basin
Lau basin
Loihi Seamount
Hydrogenetic
δ60/58Ni > 0
Ce/Ce* > 1
Hydrothermal
δ60/58Ni < 0
Ce/Ce* < 1
Hydrogenetic + hydrothermal
δ60/58Ni > 0
Ce/Ce* < 1

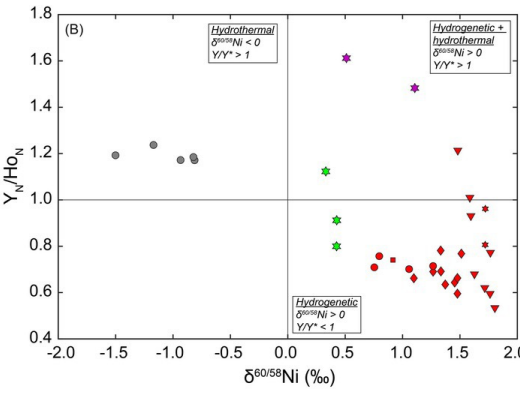
(B)
YN/HoN
δ60/58Ni (‰)
Hydrothermal
δ60/58Ni < 0
Y/Y* > 1
Hydrogenetic + hydrothermal
δ60/58Ni > 0
Y/Y* > 1
Hydrogenetic
δ60/58Ni > 0
Y/Y* < 1

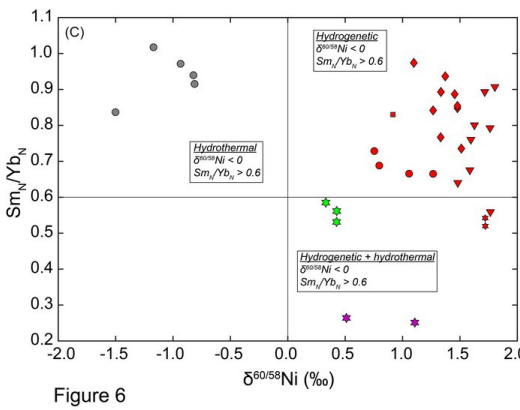
(C)
SmN/YbN
δ60/58Ni (‰)
Hydrogenetic
δ60/58Ni < 0
SmN/YbN > 0.6
Hydrothermal
δ60/58Ni < 0
SmN/YbN > 0.6
Hydrogenetic + hydrothermal
δ60/58Ni < 0
SmN/YbN > 0.6

Figure 6

Table 1: Nickel isotope composition (‰), selected elemental ratios (µg/µg) and calculated Ce anomaly (Ce/Ce*) and Y anomaly ($Y_N/Ho_N$) of Fe-Mn deposits.

| Sample Name | Location | $\delta^{60/58}Ni$ | 2se[†] | Ni/Mn | Fe/Mn | Cu/Mn | Zn/Mn | Co/Mn | Ce/Ce*[††] | $Y_N/Ho_N$ |
|---|---|---|---|---|---|---|---|---|---|---|
| ***Bulk Fe-Mn crusts*** | | | | | | | | | | |
| CAP BREST 03-03 | Ascension FZ | 1.40 | 0.03 | 0.010 | 1.87 | 0.0061 | 0.0036 | 0.023 | 2.03 | 0.78 |
| DR01-003 4-B-5 | VEMA FZ | 1.48 | 0.02 | 0.017 | 1.70 | 0.0080 | 0.0039 | 0.026 | 2.32 | 0.64 |
| DR-01-005 16-A-12 | VEMA FZ | 1.37 | 0.02 | 0.015 | 1.51 | 0.0061 | 0.0036 | 0.038 | 2.48 | 0.69 |
| DR01-005 16-A-6 | VEMA FZ | 1.51 | 0.04 | 0.017 | 1.63 | 0.0071 | 0.0040 | 0.022 | 2.28 | 0.81 |
| DR01-005 16-B-11 | VEMA FZ | 1.45 | 0.02 | 0.015 | 1.52 | 0.0051 | 0.0036 | 0.028 | 2.51 | 0.69 |
| DR01-005 16-B-12 | VEMA FZ | 1.33 | 0.02 | 0.014 | 1.38 | 0.0047 | 0.0036 | 0.036 | 2.86 | 0.74 |
| DR01-005 6-C-13 | VEMA FZ | 1.33 | 0.02 | 0.015 | 1.27 | 0.0052 | 0.0037 | 0.039 | 3.24 | 0.82 |
| DR03-003 17-C-4 | VEMA FZ | 1.27 | 0.02 | 0.014 | 1.67 | 0.0048 | 0.0042 | 0.025 | 2.37 | 0.73 |
| DR03-025 15#5 | VEMA FZ | 1.10 | 0.02 | 0.013 | 1.64 | 0.0055 | 0.0040 | 0.022 | 2.33 | 0.72 |
| DR03-025 15-D-10 | VEMA FZ | 1.48 | 0.02 | 0.015 | 1.78 | 0.0075 | 0.0044 | 0.025 | 2.41 | 0.70 |
| DR12-24 32-A-6 | Gloria FZ | 1.27 | 0.02 | 0.015 | 1.50 | 0.0068 | 0.0044 | 0.021 | 3.32 | 0.75 |
| DR12-24 32-B-2 | Gloria FZ | 0.76 | 0.02 | 0.014 | 1.35 | 0.0056 | 0.0038 | 0.030 | 3.43 | 0.74 |
| DR12-24 32-B-3 | Gloria FZ | 0.80 | 0.02 | 0.014 | 1.49 | 0.0067 | 0.0043 | 0.028 | 3.46 | 0.79 |
| DR24-09 34-A-2 | Azores TJ | 1.73 | 0.02 | 0.023 | 0.39 | 0.0023 | 0.0023 | 0.047 | 3.28 | 0.79 |
| DR24-09 34-C-2 | Azores TJ | 1.73 | 0.02 | 0.022 | 0.40 | 0.0030 | 0.0024 | 0.054 | 3.22 | 0.93 |
| J2-480-R11 | Apuupuu | 1.48 | 0.03 | 0.023 | 0.90 | 0.0069 | 0.0035 | 0.015 | 3.49 | 1.21 |
| J2-480-R11b | Apuupuu | 1.76 | 0.03 | 0.012 | 0.73 | 0.0028 | 0.0025 | 0.029 | 3.48 | 0.77 |
| J2-480-R13A | Apuupuu | 1.72 | 0.03 | 0.018 | 0.81 | 0.0080 | 0.0027 | 0.022 | 1.99 | 0.66 |
| J2-480-R13A | Apuupuu | 1.80 | 0.03 | 0.015 | 0.69 | 0.0085 | 0.0025 | 0.021 | 1.93 | 0.57 |
| J2-480-R13Ab | Apuupuu | 1.76 | 0.03 | 0.009 | 0.67 | 0.0084 | 0.0025 | 0.024 | 2.28 | 0.63 |
| J2-480-R13B | Apuupuu | 1.63 | 0.04 | 0.021 | 1.18 | 0.0012 | 0.0036 | 0.028 | 1.91 | 0.71 |
| J2-480-R14 | Apuupuu | 1.60 | 0.03 | 0.016 | 0.65 | 0.0066 | 0.0029 | 0.017 | 3.23 | 0.96 |
| J2-480 | Apuupuu | 1.59 | 0.03 | 0.013 | 0.67 | 0.0067 | 0.0031 | 0.016 | 3.88 | 1.02 |
| **Average Apuupuu Fe-Mn crusts** | | 1.67 | - | 0.016 | 0.79 | 0.0061 | 0.0029 | 0.021 | 2.77 | 0.82 |
| ***Bauer Basin Fe-Mn deposits*** | | | | | | | | | | |
| Y73-3-22D crust | Bauer Basin | 0.33 | 0.02 | 0.035 | 0.98 | 0.020 | 0.0047 | 0.005 | 0.67 | 1.10 |
| Y73-2-22D Mn NOD-1 | Bauer Basin | 0.42 | 0.03 | 0.052 | 0.44 | 0.019 | 0.0046 | 0.004 | 0.80 | 0.80 |
| Y73-3-22D MnNOD-4 | Bauer Basin | 0.43 | 0.02 | 0.030 | 0.20 | 0.015 | 0.0060 | 0.002 | 0.55 | 0.90 |
| **Average Atlantic Ocean[††††]** | | - | - | 0.018 | 1.44 | 0.0059 | 0.0042 | 0.025 | - | - |
| **Average CCZ nodules[††††]** | | - | - | 0.046 | 0.22 | 0.0377 | 0.0048 | 0.007 | - | - |
| **Average North Pacific Prime Zone[††††]** | | - | - | 0.018 | 0.74 | 0.0043 | 0.0029 | 0.029 | - | - |
| ***Lau basin hydrothermal deposits*** | | | | | | | | | | |
| NL-10-09 | Lau Basin | 0.51 | 0.02 | 0.0001 | 0.0019 | 0.0001 | 0.0006 | 0.00002 | 0.25 | 1.56 |
| NL-20-05 | Lau Basin | 1.11 | 0.02 | 0.0003 | 0.0013 | 0.0012 | 0.0009 | 0.00009 | 0.06 | 1.42 |
| ***Loihi hydrothermal deposits*** | | | | | | | | | | |
| J2-244-SS3 | Ula Nui | nd | nd | 0.005 | 16.68 | 0.0035 | 0.0028 | 0.003 | 0.99 | 1.13 |
| J2-244-SS5 | Ula Nui | -1.49 | 0.03 | 0.006 | 10.75 | 0.0011 | nd | 0.002 | 1.05 | 1.19 |
| J2-309-SS2A | Ula Nui 2 | -0.80 | 0.02 | 0.005 | 9.15 | 0.0039 | 0.0022 | 0.002 | 0.91 | 1.19 |
| J2-309-SS2B | Ula Nui 2 | -0.81 | 0.02 | 0.008 | 13.37 | 0.0019 | 0.0019 | 0.003 | 0.91 | 1.21 |
| J2-309-SS2C | Ula Nui 2 | -0.93 | 0.02 | 0.005 | 7.81 | 0.0019 | 0.0011 | 0.003 | 0.95 | 1.19 |
| J2-313-SS1-top | Ula Nui 2 | -1.16 | 0.03 | 0.002 | 3.61 | 0.0013 | 0.0005 | 0.001 | 0.95 | 1.25 |
| J2-313-SS2 | Ula Nui 2 | -1.07 | 0.02 | 0.002 | 6.73 | 0.0005 | 0.0004 | 0.002 | nd | nd |
| J2-477-SS black-green | Ula Nui | -1.16 | 0.03 | 0.003 | 2.84 | 0.0003 | 0.0006 | 0.002 | nd | nd |
| ***Bulk manganese nodules USGS*** | | | | | | | | | | |
| NOD-A-1 | Atlantic | 1.03 | 0.02 | 0.026 | 0.57 | 0.0063 | 0.0035 | 0.019 | nd | nd |
| NOD-A-1[†††] | Atlantic | 1.06 | 0.03 | 0.027 | 0.58 | 0.0063 | 0.0037 | 0.019 | nd | nd |
| NOD-P-1 | Pacific | 0.36 | 0.03 | 0.037 | 0.19 | 0.0415 | 0.0055 | 0.008 | nd | nd |
| NOD-P-1[†††] | Pacific | 0.37 | 0.03 | 0.038 | 0.19 | 0.0407 | 0.0055 | 0.008 | nd | nd |

[†]2se corresponds to a two-standard error of the mean calculated on the 50 measurement cycles through MC-ICP-MS and corrected using double-spike.

[††]$Ce/Ce^* = Ce_N/((Pr_N^2)/Nd_N)$, where subscript N stands for normalized values to PAAS.

[†††]Digestion duplicate.

[††††]Data from Hein et al. (2013).

nd: data not determined.